Structures of enveloped virions determined by cryogenic electron microscopy and tomography : Advances in Virus Research

Stass, Robert

Academic Press
2019-08-01

Stass , R , Ng , W M , Kim , Y C & Huiskonen , J T 2019 , Structures of enveloped virions determined by cryogenic electron microscopy and tomography : Advances in Virus Research . in F A Rey (ed.) , Complementary Strategies to Study Virus Structure and Function . vol. 105 , Advances in Virus Research , Academic Press , pp. 35-71 . https://doi.org/10.1016/bs.aivir.2019.07.009

http://hdl.handle.net/10138/311222
https://doi.org/10.1016/bs.aivir.2019.07.009

acceptedVersion

Structures of enveloped virions determined by cryogenic electron microscopy and tomography

Robert Stass[1,*], Weng M. Ng[1,*] , Young Chan Kim[1,*] and Juha T. Huiskonen[1,2,*,#]

[1] Division of Structural Biology, Wellcome Centre for Human Genetics, Roosevelt Drive, OX3 7BN, University of Oxford, UK

[2] Helsinki Institute of Life Science HiLIFE and Research Programme in Molecular and Integrative Biosciences, Faculty of Biological and Environmental Sciences, Viikinkaari 1, 00014, University of Helsinki, Finland

[*] These authors contributed equally

[#] Correspondence should be addressed to J.T.H (juha.huiskonen@helsinki.fi)

Abbreviations

Bundibugyo virus (BDBV)
Charge coupled device (CCD)
Chikungunya virus (CHIKV)
Contrast transfer function (CTF)
Cryogenic electron microscopy (cryo-EM)
Dengue virus (DENV)
Deoxyribonucleic acid (DNA)
Direct electron detector (DED)
Ebola virus (EBOV)
Eastern equine encephalitis virus (EEEV)
Endosomal sorting complex required for transport (ESCRT)
Enterovirus 71 (EV71)
Focused ion beam (FIB)
Glycoprotein (GP)
Hazara virus (HAZV)
Hemagglutinin (HA)
Hepatitis B virus (HBV)
Human immunodeficiency virus (HIV)
Human parainfluenza virus 3 (HPIV3)
Japanese encephalitis virus (JEV)
Lassa virus (LASV)
Major capsid protein (MCP)
Marburg virus (MARV)
Measles virus (MeV)
Mouse hepatitis virus (MHV)
Mucin-like domain (MLD)

Neuraminidase (NA)
Newcastle disease virus (NDV)
Nucleocapsid (NC)
Human parechovirus 3 (HPeV3)
Ribonucleic acid (RNA)
Rift Valley fever virus (RVFV)
Severe acute respiratory syndrome-related coronavirus (SARS-CoV)
Semliki Forest virus (SFV)
Sendai virus (SeV)
Sindbis virus (SINV)
Single particle averaging (SPA)
Stable signal peptide (SSP)
Sub-tomogram averaging (STA)
Tick borne encephalitis virus (TBEV)
Tula virus (TULV)
University of Helsinki virus (UHV)
Vaccinia virus (VACV)
Venezuelan equine encephalitis virus (VEEV)
Vesicular stomatitis virus (VSV)
Virus-like particle (VLP)
Volta phase plate (VPP)
West Nile virus (WNV)
Zika virus (ZIKV)

Keywords: cryogenic electron microscopy, cryo-EM, tomography, cryo-ET, virion, enveloped virus, membrane-containing virus, single particle averaging, sub-tomogram averaging, viral glycoprotein, viral fusion, membrane fusion, virion budding

1. Introduction

Enveloped viruses encompass a large group of viruses with different morphologies and genome types spanning across different virus families infecting host cells from all three domains of life (Eukaryota, Bacteria and Archaea). Common to all of these viruses is that their virions harbor a lipid bilayer which associates with integral and peripheral membrane proteins. Together these structural components create a viral envelope that encloses the genome, or an internal protein–genome complex called the nucleocapsid (NC). The virion envelope is derived from the host cell membrane by fission in the budding process of progeny virions. During entry to a new host cell, it must fuse to a host cell membrane for the enclosed genome or the NC to enter the cytoplasm. This process is catalysed by membrane fusion proteins (Harrison, 2015; Kielian, 2014).

Understanding the structures of enveloped viruses is important for understanding their infection mechanisms, especially entry by membrane fusion in addition to assembly and budding by membrane fission. Various types of enveloped virus morphologies are schematized in Figure 1. The shapes of the enveloped virions range from spherical or icosahedral to ellipsoidal to pleomorphic and filamentous. The virion envelope surface is covered to varying degrees by membrane proteins that often form multimeric assemblies.

Such morphological units on the virion surface are referred to as capsomers or spikes, as they often protrude from the surface and have pointed appearance. In animal viruses, these surface proteins are typically glycosylated (glycoproteins; GPs). In a seminal study on herpes simplex virus 1 (HSV-1) the GPs were visualized on the virion surface by cryo-electron tomography (cryo-ET) (Grunewald, 2003). The capsomers may further form higher order assemblies which may have local symmetry. In many enveloped viruses the lipid bilayer is almost entirely covered by surface proteins, leaving hardly any naked membrane accessible from the virion exterior. This is the case for example in the members of *Flaviviridae*, such as DENV, where GPs form a continuous icosahedral protein shell on the envelope (Kuhn et al., 2002), and members of *Hantaviridae*, such as Tula virus (TULV), where GPs form locally ordered patches on the envelope (Huiskonen et al., 2010). In contrast, members of *Retroviridae*, such as HIV, harbor very few glycoprotein spikes, leaving a large fraction of the membrane naked (Briggs et al., 2003). Some enveloped viruses harbor a symmetric nucleocapsid, which can have either icosahedral or helical symmetry. For example, members of *Togaviridae*, such as Semliki Forest virus (SFV), harbor an icosahedrally symmetric nucleocapsid (Fuller et al., 1995). Finally, many, but not all, enveloped viruses have a matrix protein directly under the envelope (Ke et al., 2018a; Li et al., 2016a).

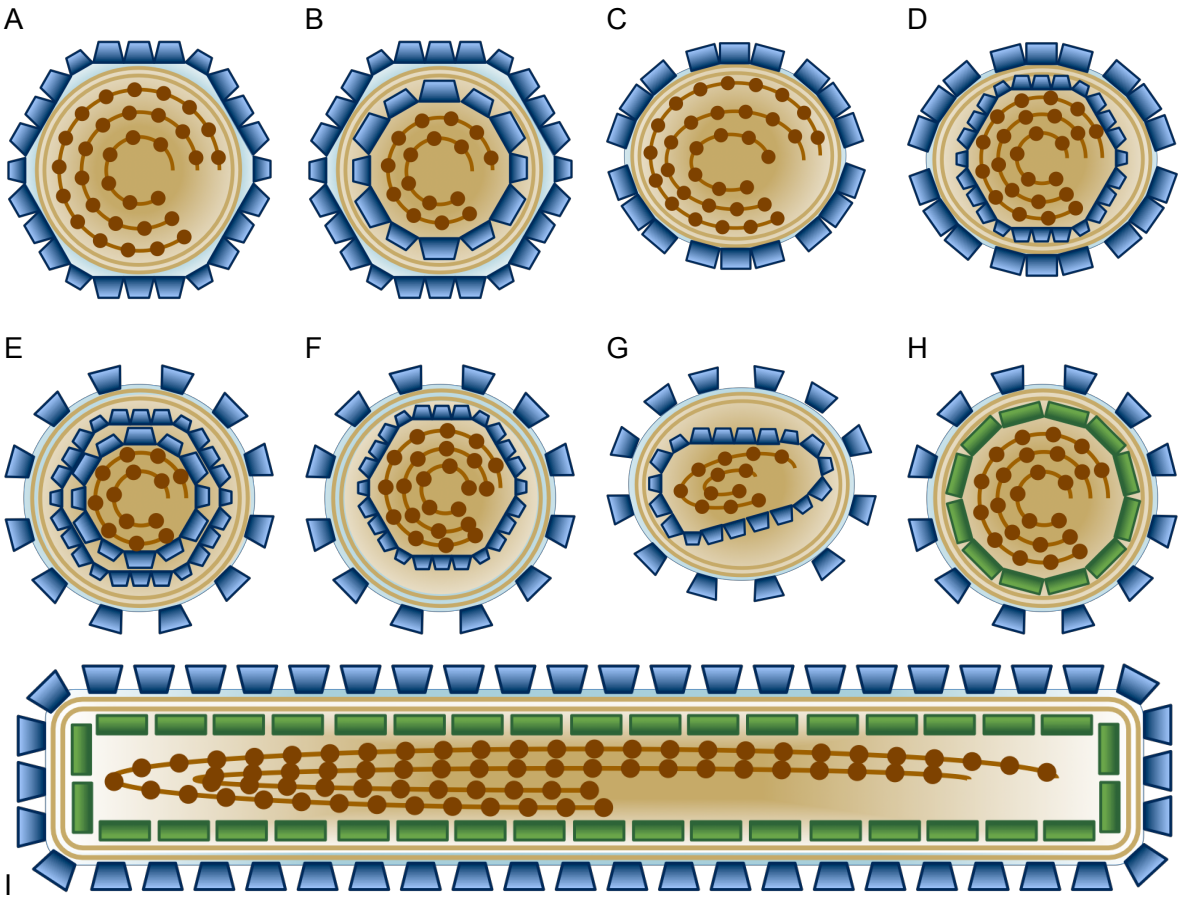

Figure 1. Approximate schematic presentations of different types of enveloped virion morphologies. (A) Virion with an icosahedrally symmetric outer protein shell covering a lipid bilayer. Example structures include members of *Flaviviridae* such as dengue virus (DENV) (Kuhn et al., 2002) and *Phenuiviridae* such as Rift Valley fever virus (RVFV) (Huiskonen et al., 2009) in addition to many membrane-containing prokaryotic viruses including members of *Tectiviridae* such as bacteriophage

PRD1 (San Martín et al., 2002). (B) Virion with an icosahedrally symmetric outer protein shell covering a lipid bilayer and an additional icosahedrally symmetric inner protein shell. Example structures include members of *Togaviridae* such as SFV (Mancini et al., 2000). (C) A virion with a non-icosahedrally symmetric, but locally ordered outer protein shell covering most of the lipid bilayer and lacking a matrix layer. Example structures include members of order *Bunyavirales* such as Tula virus (TULV) (*Hantaviridae*) (Huiskonen et al., 2010), Hazara virus (HAZV) (*Nairoviridae*) (Punch et al., 2018) and Bunyamwera virus (BUNV) (*Orthobunyaviridae*) (Bowden et al., 2013). (D) A virion with an icosahedral inner capsid and a non-icosahedrally symmetric, but locally ordered outer protein shell. Example structures include members of *Hepadnaviridae* such as hepatitis B virus (HBV) (Dryden et al., 2006). (E) A virion with two internal icosahedrally symmetric protein shells surrounded by a lipid envelope with surface spikes. Example structures include members of *Cystoviridae* such as bacteriophage Φ6 (Jäälinoja et al., 2007a). (F) Members of *Herpesviridae*, such as HSV-1 (Grunewald, 2003), have an icosahedrally symmetric protein shell, enclosed by a tegument layer (not shown) and an external lipid envelope with surface glycoproteins. (G) Some members of *Retroviridae*, such as human immunodeficiency virus 1 (HIV-1) (Briggs et al., 2006), have mature virions with relatively few GPs on the virion envelope. (H) A virion with a lipid bilayer, decorated by glycoprotein spikes and an internal matrix protein layer is shown. Examples include members of *Arenaviridae* such as Lassa virus (LASV) (Li et al., 2016a)*, Coronaviridae* such as severe acute respiratory syndrome-related coronavirus (SARS-CoV) (Neuman et al., 2006), and *Paramyxoviridae* such as measles virus (MeV) (Ke et al., 2018a). (I) A filamentous virion with envelope glycoprotein spikes and internal matrix layer. Examples include members of *Filoviridae*, such as Ebola virus (EBOV) (Bharat et al., 2012) and *Pneumoviridae* such as respiratory syncytial virus (RSV) (Ke et al., 2018b), in addition to filamentous forms of influenza A virus (*Orthomyxoviridae*) (Calder et al., 2010). Blue, viral structural protein; Light brown, lipid bilayer; Brown circles, nucleoprotein or other genome-associated protein; Brown line(s), viral genome segment(s); Green, matrix protein. Note that we have not attempted to accurately depict the genome type nor its organization or the symmetry and arrangement of different protein shells.

In this chapter we review recent advances in understanding enveloped virus structures by cryogenic electron microscopy (cryo-EM). We will begin by an overview of different cryo-EM data collection and processing strategies relevant to the topic and then proceed to reviewing how cryo-EM structures of enveloped virions contribute to our understanding of the molecular interactions driving assembly, the dynamic nature of viral particles, their budding and membrane fusion mechanisms in addition to virus neutralization and furthermore how these structural biology studies are informing vaccine design.

2. Cryogenic electron microscopy in membrane virus research

Cryo-EM is a well-suited method for the structural analysis of enveloped virions (Subramaniam et al., 2007). As the structures are often pleomorphic (*i.e.* lacking a regular shape), they are often not amenable to X-ray crystallography, another structural biology technique which relies on crystallization of the sample of interest. In fact, in only a few cases has the structure of an enveloped virion been solved by X-ray crystallography (Abrescia et al., 2004, 2008). Cryo-EM methods, however, are applicable to both regular and pleomorphic virions, as no crystals are needed and structures can be determined from a relatively small amount of purified virions. The electric potential maps (or simply 'cryo-EM density maps') determined by cryo-EM have in many cases similar level of detail when compared to electron density maps determined by X-ray crystallography, although there are also subtle differences that become more significant at high resolution (Wang and Moore, 2017). Furthermore, cryo-EM allows structural investigations of more complex and rapid

processes such as viral envelope–host membrane fusion and viral budding from the plasma membrane of infected cells.

As many enveloped viruses are human and animal pathogens, their production, purification and preparation for cryo-EM requires suitable containment facilities and bio-safety protocols (Sherman et al., 2013). To circumvent the need for decontaminating cryo-EM equipment, which may be in some cases impractical, purified virions can be inactivated for example by chemical fixation (Bharat et al., 2011; Halldorsson et al., 2018; Li et al., 2016a) or ultraviolet radiation (Park et al., 2011; Ye et al., 2018; Zhong et al., 2016) prior to cryo-EM sample preparation. Alternatively, virus-like particles (VLPs) that contain the relevant viral structural proteins with a lipid bilayer can be used as a model system instead of the native virion (Li et al., 2016a; Sun et al., 2013). Whether live or inactivated, virion or VLP, purified particles are prepared for cryo-EM similar to any other macromolecular complex (Thompson et al., 2016). A small aliquot of virus suspension, typically 3 µl, is pipetted on an EM sample grid, a circular metal mesh (3 mm in diameter), typically coated with a foil of holey carbon or gold. The grid, held by tweezers, is then blotted by a piece of filter paper to remove most of the sample in order to leave a very thin film of virus suspension on the grid (often not much thicker than the particle itself). The grid is then plunged in liquid ethane, which is cooled by liquid nitrogen. The extremely cold temperature of the cryogen (around –180^{o}C) leads to a very rapid cooling rate, and the formation of amorphous, glass-like ice, which is compatible with the vacuum of the electron microscope column and also transparent to the electron beam.

Typical cryo-EM data collection and processing workflows for enveloped viruses are outlined in Figure 2. Cryo-EM data can be collected either as 2D projection images (micrographs; Figure 2A) or as a series of tilted images (a tomographic tilt series) from which a 3D tomographic volume (or a tomogram) can be calculated (Figure 2B). To increase the inherently low signal-to-noise ratio (SNR), signal from multiple images (or volumes) needs to be averaged in a coherent manner to reach sufficiently high resolution in the average. The target resolution depends on the types of questions addressed and ranges from better than 3 Å (required to model the polypeptide chains of proteins and to see small bound molecules) to 30 Å and even lower (sufficient for addressing the organisation of envelope proteins and visualising the lipid bilayers; Table 1). Different approaches to averaging in the context of enveloped viruses are discussed below.

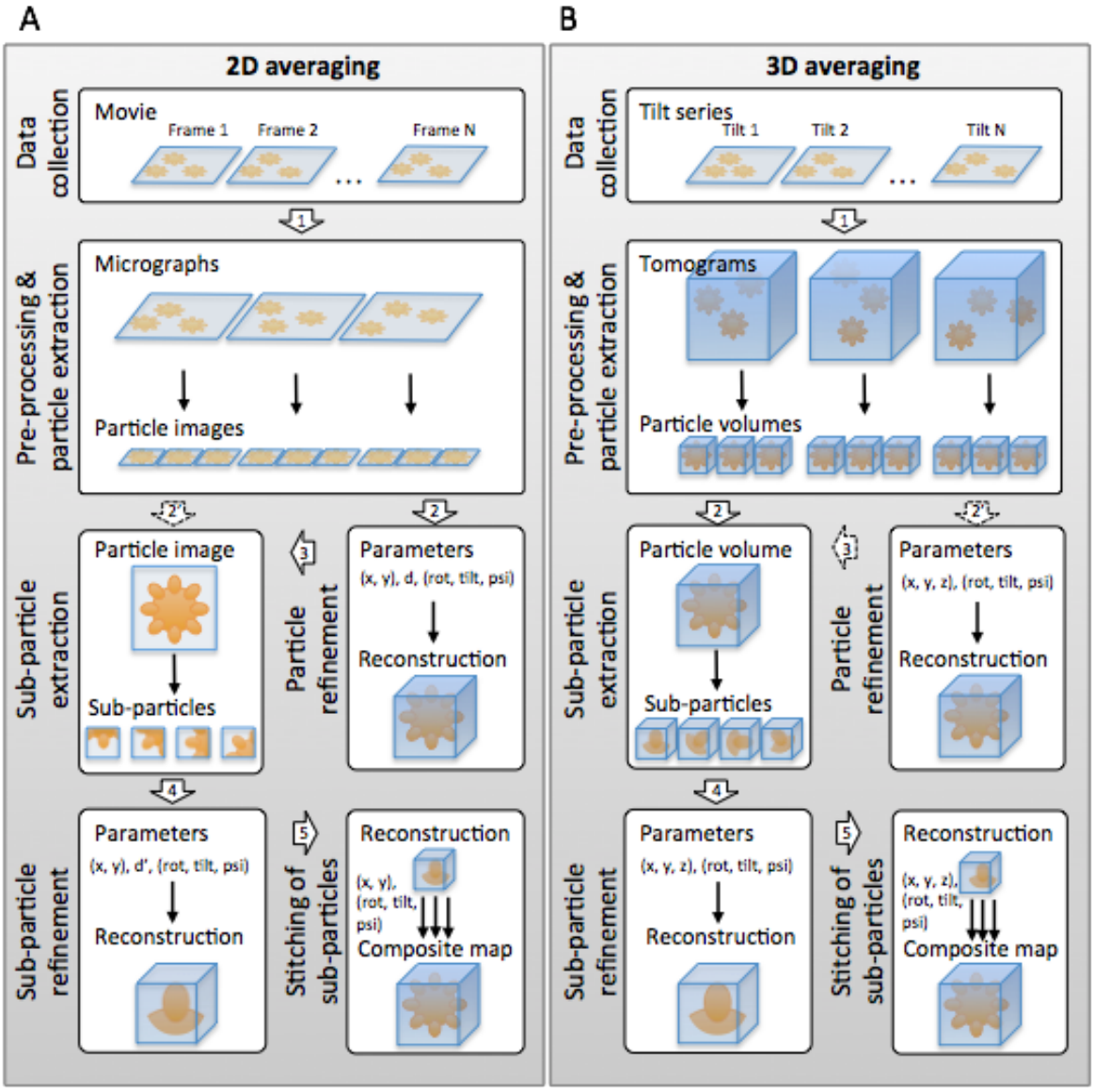

Figure 2. Cryo-EM data processing strategies for determining structures of enveloped virions and their glycoprotein spikes. (A) Here an enveloped virion is depicted as an orange sphere with protruding blobs that depict glycoprotein spikes. Defocus of the particle is d. Defocus of the sub-particle is d'. The view direction of the particle or sub-particle is defined by angles rot and tilt. The in-plane rotation of the particle projection is defined by psi. (B) Note that each image in a tomography tilt series is potentially recorded first as a movie. The range between tilt 1 to tilt N is typically [–60,60 degrees] and N is typically 41 (for 3-degree angular sampling) or 61 (for 2 degree angular sampling). Here and in the text we have assumed that the tomograms have been corrected for the effects of the contrast transfer function (CTF) during preprocessing but other approaches are possible. Here the three Euler angles (rot, tilt, psi) define the orientation of the particles and the sub-particles. The block arrows refer to different data processing steps described in the text. The block arrows with dashed outlines depict less common data processing approaches.

2A. Single particle averaging and localized reconstruction

Many enveloped viruses harbor an icosahedrally symmetric protein shell, which can be either external (Figure 1A) or internal to the lipid bilayer (Figure 1D,F). Some enveloped virions have two such shells sandwiching the lipid bilayer (Figure 1B) and some have two

internal shells (Figure 1E). The structures of the icosahedrally symmetric protein shells in these types of virions can be determined by cryo-EM and single particle averaging (SPA). In standard SPA workflows, the virions are located in the micrographs (particle picking) and extracted in smaller images each containing one virion image in the middle (particle images). After determining the defocus value of each particle image, the exact location of the virion in the image (two coordinates) and orientation of the particle (three angles), the structure of the virion can be determined (or reconstructed) (Figure 2A; steps 1 and 2). To increase the SNR and thus attainable resolution for the protein shells, icosahedral symmetry is normally applied at this stage. Several icosahedrally symmetric enveloped virus structures have been determined by this approach (see section 3A; Table 1). To obtain the highest possible resolution for large membrane viruses, it may also be crucial to take into account the thickness of the specimen in the 3D reconstruction process (Wolf et al., 2006).

The downside of this standard SPA workflow is that those components of the virion that are not organized in a strictly symmetric fashion will get incoherently averaged and this limits the attainable resolution, or hinders their reconstruction all together (Huiskonen, 2018). For example, if the structure of a virion presented in Figure 1A is somewhat flexible, signal both between different particles and asymmetric units within each particle will be incoherently averaged. In order to improve the resolution for flexible enveloped virions and their symmetry-mismatched components, the localized reconstruction method can be used to divide the particle in several sub-particles (Figure 2A; sub-particle extraction) (Huiskonen, 2018; Ilca et al., 2015). The orientation (three angles: ro: tilt and psi) of each sub-particle and location in the particle image (two coordinates: x and y) can then be calculated and used as an initial estimate to further refine sub-particles around their original positions and locations (Figure 2A; steps 1, 2, 3, and 4). Furthermore, the defocus of each sub-particle is calculated to take into account the defocus gradient across the specimen (Ilca et al., 2015). This approach has allowed improving the resolution of Rift Valley fever virus (RVFV) virions that have an icosahedrally ordered, but yet highly flexible, large protein shell (diameter ~110 nm), from 13 Å to 7.7 Å (Halldorsson et al., 2018). The resolution in this study and other similar studies may be limited due to overlaps between other subparticles, the membrane and the genome. In some cases overlapping components can be subtracted from the particle image by partial signal subtraction to improve the accuracy of sub-particle alignments (Bai et al., 2015; Huiskonen et al., 2007). Also it is worth noting that in this approach only distortions in the image plane can be handled and any movement along the beam direction (corresponding to further changes in defocus) is ignored. After aligning sub-particles in the image plane and reconstructing them, a composite 3D model of the virion can be created by 'stitching' the entire virion from individual sub-particle reconstructions (Figure 2A, step 5). Recently the structure of the complete Sindbis virus (SINV) virion has been reconstructed this way from three separate sub-particle reconstructions at 3.5 Å resolution (Chen et al., 2018).

Some particles are too pleomorphic for even rough orientational alignment rendering them challenging for SPA approaches. Several studies have attempted averaging glycoprotein spikes from the edge of an pleomorphic particles (Figure 2A; steps 1 and 2'). This has been done for example for HNTV (Battisti et al., 2010), DENV at acidic pH (Zhang et al., 2015), and SARS (Neuman et al., 2006). In contrast to localized reconstruction where the three angles describing the orientation of the sub-particle (rot, tilt and psi) can be estimated from the orientation parameters of the entire particle, in this approach only two angles of the three

angles (tilt and psi) can be estimated (tilt can be assumed to be close to 90 degrees; psi can be estimated from the normal of the membrane projection). Due to this limitation, it is not possible to calculate a 3D reconstruction without further exhaustive alignment to determine the third angle that is unknown (rot). Another limitation of this approach is that spikes at the edge of the particle can overlap other spikes and in the absence of an approximate 3D model of the particle, these overlaps cannot be removed by partial signal subtraction (Bai et al., 2015; Huiskonen et al., 2007). Due to these reasons, most studies have classified and averaged spike side-view projections only in 2D (Figure 2A; steps 1 and 2'). At the 2D level, such studies have been informative. For example, two distinct conformations of the SARS M protein were observed by this approach (Neuman et al., 2006). In some cases 3D averaging has also been performed (Figure 2A; step 4). In one example, the 3D structure of the tetrameric GP spike of HNTV was resolved to 25 Å from side-view sub-particles (Battisti et al., 2010)(Figure 2A; steps 1, 2' and 4). This structure agreed well with the structure of TULV GP spike solved by cryo-ET and sub-tomogram averaging (STA)(Huiskonen et al., 2010). In another example, the structure of the trimeric GP spike of Ebola virus (EBOV) was determined at 11 Å resolution from side-view projections on the virion surface (Beniac and Booth, 2017)(Figure 2A; steps 1, 2' and 4). Consistent with a cryo-ET and STA investigation of GP from EBOV VLP (Tran et al., 2014), a mucin-like domain (MLD) was located to the apex and sides of each GP1 monomer, partially shielding the receptor-binding site, while the GP1 sits atop the GP2. In these side-view averaging approaches it is only possible to include spikes from the edge of the virion projection image so the the packing of the spikes on the virion surface remains unattainable.

2B. Tomography and sub-tomogram averaging

Tomography is a method well suited for determining structures of flexible and truly pleomorphic virions from cryo-EM data that are challenging or unsuitable for the SPA approaches described above. When virions lack well defined shape, it is impossible to combine particles with different views extracted from 2D micrographs to reconstruct a correct 3D volume. Instead, different views must be collected for each virion in the form a series of tilted images (Figure 2B). These views are then combined to calculate a tomographic 3D volume (a tomogram) of the specimen region under investigation. Due to the slab-shaped geometry of the cryo-EM specimen holders and the cryo-EM grid itself, the specimen cannot be tilted to 90 degrees and thus the angular range in a typical tomographic tilt series is limited from –60 to +60 degrees. This results in incomplete sampling of information in the 3D reconstruction, which can be described as a 'missing wedge' in the 3D Fourier transform of the tomogram. Because of this limitation, features in tomograms are distorted and averaging of 3D particles in different orientations is required to fully sample the information in the final 3D reconstruction (Subramaniam et al., 2007).

Similar to the 2D processing workflow described in the previous section, it is often practical to extract smaller 3D volumes, each corresponding to a single virion, from the larger tomograms (Figure 2B; particle extraction). If these 3D particles are homogenous enough it is then in possible to align, classify and average them together. For example, the first low-resolution structure of a bunyavirus (Uukuniemi virus, UUKV; *Phenuiviridae*) was determined by aligning single 3D volumes of virions and by applying icosahedral symmetry (Overby et al., 2008) (Figure 2B; steps 1 and 2'). Once the orientation (rot, tilt, psi) of each particle is known from an initial alignment, it is possible to deal with any possible flexibility of the virion

by extracting 3D sub-particles (also referred to as sub-volumes or sub-tomograms; Figure 2B; step 3)(Castaño-Díez et al., 2017). These sub-particles, corresponding for instance to envelope GP spikes can then be refined further (Figure 2B; step 4) and finally a composite map of the entire virion can be stitched from the 3D reconstruction of the sub-particles (Figure 2B; step 5)(Huiskonen et al., 2010).

In most cases where tomography is applied, however, the 3D particles are too dissimilar to be aligned an averaged in coherent manner. This is the case with with truly pleomorphic virions. In these cases, sub-particles of GP spikes are extracted from unaligned 3D volumes of enveloped virions (Figure 2B; steps 1 and 2). The locations of the spikes first need to be determined by a 3D search, which can be restricted close to the membrane surface (Castaño-Díez et al., 2017; Huiskonen et al., 2014). Also the direction of the spike can be estimated from the membrane surface normals. Once the 3D-subvolumes, each corresponding to a centered spike, have been extracted, only the rotation around spike long axis remains to be determined before a 3D reconstruction of the sub-particle can be calculated (Figure 2B, step 4)(Förster et al., 2005; Zanetti et al., 2006). For example, several studies have produced low resolution reconstructions of Env from native HIV virions using STA (Liu et al., 2008; Zanetti et al., 2006; Zhu et al., 2003, 2006). As described above, these 3D sub-particle reconstructions can then plotted back onto the original particle volumes to stitch together composite models of entire virions. Here, the completeness of this stitching depends on the coverage of the 3D picking (Huiskonen et al., 2010).

2C. Hybrid methods

As we have outlined in Figure 2, averaging of 2D and 3D single particles follow highly analogous workflows. In some cases it may be beneficial to mix these two. In one example of such a hybrid approach, the structure of the GP spike of prototypic foamy virus (PFV) has been studied (Effantin et al., 2016). First STA was used to determine the structure of the trimeric GP at ~30 Å resolution (Figure 2B; steps 1, 2, 3, 4). Plotting back the GP structure allowed visualizing hexagonal assemblies of six GPs on the envelope (Figure 2B; step 5). A patch of six trimers was extracted, six-fold symmetry was imposed and this volume was used as a search model to pick and extract GP sub-particles directly from untilted images (Figure 2A; steps 1 and 2'). GP spike sub-particles were then subjected to conventional SPA refinement that allowed determination of a three-fold symmetrized GP density map at ~9 Å. The density map revealed a region interpreted as a coiled-coil of three α-helices, a hallmark of viral class I fusion proteins.

3. Structures of purified virions

3A. Virions with icosahedral symmetric protein shells

Structures of iicosahedrally symmetric proteins shells in enveloped virions have been a topic of several cryo-EM studies over the past two decades. The first 3D reconstructions of Semliki Forest virus (SFV; *Togaviridae*) and dengue virus (DENV; *Flaviviridae*) virions were determined at 22 Å resolution (Fuller et al., 1995) and at 24 Å resolution (Kuhn et al., 2002), respectively, by SPA with icosahedral symmetry applied (Figure 2A; steps 1 and 2). At such limited resolution only the rough morphology of the virions could be resolved. However, fitting of X-ray structures into cryo-EM maps has, in many cases, allowed the creation of so-

called pseudo-atomic models of the glycoprotein shells. For example, fitting of the X-ray crystallographic structure of the E protein from another flavivirus, tick borne encephalitis virus (TBEV)(Rey et al., 1995) revealed the so-called herringbone arrangement of E-protein dimers on the DENV virion surface (Kuhn et al., 2002). The advent of direct electron detectors (DEDs) and other advances in electron microscope hardware and image processing software led to a 'resolution revolution' in cryo-EM making it possible to derive atomic models from cryo-EM maps of single particles alone (Kühlbrandt, 2014). A notable exception from the pre-resolution revolution era of cryo-EM is the structure of mature DENV that was determined at 3.5 Å resolution from images collected on a charge coupled device (CCD) camera (Zhang et al., 2013a).

In the post resolution revolution era, determining structures of icosahedrally symmetric protein shells in enveloped viruses from cryo-EM data alone has become routine. For instance, the structure of mature Zika virus (ZIKV; *Flaviviridae*) virion has been solved by cryo-EM and SPA by two research groups at ~3.8 Å resolution (Kostyuchenko et al., 2016; Sirohi et al., 2016). These studies revealed that despite the high level of structural similarity to other flaviviruses such as DENV, ZIKV particles displayed greater thermal stability at higher temperature (40^{o}C degrees) which could account for their survival in the semen and urine. ZIKV protein shell also presents a unique amino acid region around the Asn154 glycosylation site which may explain the neurotropic nature of ZIKV similar to West Nile virus (WNV; *Flaviviridae*). A recent 4.3-Å cryo-EM structure of Japanese encephalitis virus (JEV; *Flaviviridae*) has allowed mapping of neurovirulence factors on the virus surface (Wang et al., 2017). The same strategy has been applied to several members of the *Togaviridae* family. A cryo-EM structure of Sindbis virus (SINV; *Togaviridae*) at 3.5 Å resolution has allowed the identification of a 'pocket factor', a 20-Å long molecule, possibly a phospholipid tail, projecting from the viral lipid bilayer into a membrane-proximal hydrophobic pocket of the GP shell (Chen et al., 2018). A chikungunya virus (CHIKV; *Togaviridae*) VLP structure has been determined at 5.3-Å resolution. This study shows that togavirus VLPs reflect the structures of mature virions and revealed that CHIKV E1 and E2 glycoproteins are not associated with the E3 glycoprotein unlike other alphaviruses such as Venezuelan equine encephalomyelitis virus (VEEV) (Sun et al., 2013).

Structures of several prokaryotic viruses with icosahedral capsids and an internal membrane have also been studied by cryo-EM and SPA. Typically these viruses harbor major capsid proteins (MCPs) that consist of upright beta-barrel folds and fully cover an internal membrane following different arrangements (described by the triangulation [*T*] number). These viruses include bacteriophages PRD1 (*T*=25) (San Martín et al., 2002), Bam35 (*T*=25) (Laurinmäki et al., 2005), PM2 (*T*=21*d*) (Huiskonen et al., 2004) and FLiP (*T*=21*d*) (Laanto et al., 2017), in addition to archaeal viruses SH1 (*T*=28) (de Colibus et al., 2019), STIV (*T*=31*d*) (Veesler et al., 2013) and STIV2 (*T*=31*d*) (Happonen et al., 2010). Similarity of the MCP fold and the arrangement MCPs of the virions surface have allowed grouping these viruses to a so-called 'PRD1–adenovirus lineage', based on the extended similarity to the non-enveloped adenovirus. Interestingly, cryo-EM and SPA has revealed that giant eukaryotic dsDNA viruses share the same basic MCP building block with aforementioned prokaryotic viruses and adenovirus. In these giant dsDNA viruses compelling evidence exists for an internal lipid bilayer (Xiao and Rossmann, 2011). Structures of several viruses belonging to this group have been determined by cryoEM and SPA, including CIV (*T*=147) (Khayat et al., 2010), PBCV-1 (*T*=169*d*) (Zhang et al., 2011), PpV01 (*T*=219*d*) (Yan et al., 2005), CroV (*T*=499)

(Xiao et al., 2017) and mimivirus (972≥T≥1,200) (Xiao et al., 2009)(Klose et al., 2010). Cryo-EM has also been used in characterizing other types of enveloped bacteriophages belonging to the *Cystoviridae* family. Members of this family have an outer lipid envelope with surface proteins enclosing two internal icosahedral protein shells (with *T*=1 and *T*=13*l* architecture) enclosing a segmented dsRNA genome. Structures including Φ6 (Jäälinoja et al., 2007b)(Sun et al., 2017), Φ8 (Jäälinoja et al., 2007b) and Φ12 (Wei et al., 2009) have highlighted structural similarities in their protein shells to non-enveloped reoviruses. Taken together these studies have started to exemplify possible distant evolutionary links between enveloped and non-enveloped viruses.

3B. Dynamic nature of enveloped virions

In addition to the high-resolution cryo-EM structures of enveloped virions and their icosahedrally symmetric protein shells, several cryo-EM studies have highlighted the dynamic nature of these shells. One realization is that enveloped virions may assemble from a fixed number of GP capsomers (such as 12 pentamers and N hexamers) on a defined icosahedral lattice but the resulting virion structure may be flexible. The first representative structure for members of *Phenuiviridae*, and for the entire order of Bunyavirales, has been studied by cryo-ET of purified UUKV virions (*Phlebovirus*, *Phenuiviridae*) (Overby et al., 2008). This study revealed that the virion has icosahedral symmetry with *T*=12 triangulation and should then in principle be amenable to SPA. Later the structure of RVFV (*Phlebovirus*, *Phenuiviridae*) virions has been studied by SPA but the resolution has been limited to 13 Å due to significant flexibility of the GP layer (Halldorsson et al., 2018). Despite this limitation, localized reconstruction method (Ilca et al., 2015) has allowed partially dealing with flexibility to improve the resolution to 7.9 Å. This was sufficient for flexible fitting of Gn and Gc X-ray crystallographic structures, revealing how the Gn chaperone protein caps the fusion loops of the fusion protein Gc (Halldorsson et al., 2018).

Highly dynamic structural changes take place during virion maturation and entry (Hasan et al., 2018a). Cryo-EM studies have played a significant role in determining the structural changes exhibited by flaviviruses in their immature, fusogenic and mature forms. The first cryo-EM structure of a mature DENV showed that the mature infectious particles are icosahedral and ~500 Å in diameter. The surface is smooth and is comprised of 90 copies of an E protein dimer that is closely packed suggesting that a major rearrangement is required before host cell fusion (Kuhn et al., 2002). Cryo-EM and crystallography of fusogenic virions has revealed how the parallel E protein dimers of the mature virion first rearrange into monomers and then into the E-protein fusogenic trimers with three-fold symmetry (Allison et al., 1995; Bressanelli et al., 2004; Modis et al., 2004; Zhang et al., 2015). The first cryo-EM studies of immature flavivirus particles (DENV and YFV) have showed striking differences in terms of the considerably larger diameter (600 Å) and the presence of 60 prominent trimeric spikes (Zhang et al., 2003b). More recently, the 9-Å resolution cryo-EM structure of the immature ZIKV has showed similar characteristics and spatial arrangement to DENV (Prasad et al., 2017). These studies demonstrate that flavivirus particles undergo a series of significant conformational changes during virion maturation and entry, reflecting the highly dynamic nature of the virions.

It is becoming increasingly clear that temperature is a significant factor in the conformation of enveloped virions, yet typically samples are prepared for cryo-EM at ambient temperature or

below. Two cryo-EM studies on the structure of the mature DENV virion have highlighted the structural changes to DENV virion at elevated temperatures (Fibriansah et al., 2013; Zhang et al., 2013b). When heated to 37^{o}C DENV envelopes change their appearance from smooth to bumpy. This suggests that nearly all mature DENV virions involved in human infection have bumpy structures and therefore optimal vaccines should target epitopes exposed on the bumpy form of the virus.

3C. Inherently pleomorphic virions and their glycoproteins

Enveloped viruses whose structural protein shells do not exhibit icosahedral symmetry present a challenge for high resolution cryo-EM structure determination as these virions are unsuitable to SPA processing. In these cases cryo-ET has been used to study the overall virion ultrastructure. Examples of such studies include those on HSV-1 (Grunewald, 2003), vaccinia virus (Cyrklaff et al., 2005), HIV (Briggs et al., 2006), influenza virus (Calder et al., 2010; Harris et al., 2006), rabies virus (Guichard et al., 2011), EBOV (Bharat et al., 2012), MARV (Bharat et al., 2012) and baculovirus (Wang et al., 2016a). These studies have provided valuable insights into the virion morphology and high-level organization of structural components. For example, cryo-ET of HIV has revealed that the virion is comprised of a protein core containing the viral genome surrounded by an envelope, in which the surface glycoprotein (Env) is embedded (Briggs et al., 2006). The HIV genome is contained within a conical capsid made up of the capsid protein CA arranged into hexamers and pentamers. Cryo-ET and STA have also been used to determine the structure of the capsid within intact virions (Mattei et al., 2016). Studies on influenza virions have revealed a capsular or a filamentous shape, with HA covering most of the virion surface and NA clustering in patches (Calder et al., 2010; Harris et al., 2006). A layer of matrix protein, M1, underneath the membrane and eight RNP segments were also observed. Interestingly, NA and RNPs occupy opposite poles of the virion (Calder et al., 2010). Like the filamentous form of influenza, EBOV (Bharat et al., 2011) and MARV (Bharat et al., 2012) also present a strikingly filamentous morphology.

The first three-dimensional characterizations of arenaviruses and their GP spikes have been performed by cryo-ET and STA of University of Helsinki virus (UHV; reptarenavirus) (Hetzel et al., 2013) and Lassa virus (LASV; mammarenavirus) (Li et al., 2016a). These studies have revealed the higher order assembly of the GP spikes, with each spike consisting of three protomers of GP1–GP2 heterodimers organized into a tripartite complex, distributed randomly over the whole virion surface. The improvement in resolution of the spike complex from 32 Å (UHV) to 14 Å (LASV) has allowed the fitting of a crystal structure of the LASV GP1–GP2 ectodomain (Hastie et al., 2017). The resulting model places the GP1 receptor-binding glycoproteins to the membrane-distal region of the spike complex where they sit atop the GP2 class I fusion glycoproteins that protrude from the virion membrane. Inspection of the tomographic slices shows that the spike complex penetrates the membrane and interacts with the underlying layer of the Z matrix protein that links the to the genome (Li et al., 2016a). Although association between stable signal peptide (SSP) and GP2 has been reported (Bederka et al., 2014; Shankar et al., 2016), the structure and topology of SSP remain unresolved at 14 Å resolution.

Cryo-ET and STA have also started to reveal the striking differences in GP multimerization and higher level clustering on the viral envelopes, several studies focusing on bunyaviruses

(*Bunyavirales*). The organisation of hantavirus GP spikes on the virion has been studied by sub-tomogram averaging of TULV (*Hantaviridae*) glycoprotein spikes, followed by placing them back to their correct positions on the virion envelope (Huiskonen et al., 2010; Li et al., 2016b). These studies showed how the tetrameric spikes, consisting of four copies of Gn–Gc heterodimers, cover the envelope surface in locally ordered patches. Improved resolution in later models allowed proposing a model where the globular domains of Gn are membrane distal with a tetrameric stalk that descends into the membrane and the Gc fusion proteins occupy the space between the spikes (Li et al., 2016b). Another prototypic bunyavirus, Bunyamwera virus (BUNV; *Orthobunyaviridae*) has been studied by cryo-ET and STA (Bowden et al., 2013). This study revealed the first low-resolution structure of the trimeric glycoprotein spikes and how these spikes create locally ordered lattices on the virion surface, analogous to TULV (Huiskonen et al., 2010). Nairoviruses are another example of a pleomorphic bunyavirus displaying an ordered lattice of glycoproteins on their envelope. The first structural insights into this lattice came from STA of HAZV revealing a tetrameric array of spikes on the virion envelope (Punch et al., 2018).

The first representation of measles virus (MeV; *Paramyxoviridae*) ultrastructure (Liljeroos et al., 2011), derived by cryo-ET of purified virions, revealed that the virus is highly pleomorphic with no obvious glycoprotein ordering and are highly variable in size (50–510 nm), agreeing with the observations of similar structural investigations of SeV (Loney et al., 2009), NDV (Battisti et al., 2012), and HPIV3 (Gui et al., 2015) virions. Although a recent crystallographic study revealed that the fusion glycoprotein is capable of forming a pseudo-hexameric arrangement (Xu et al., 2015), this organization has yet to be visualized on native virions. Human orthopneumovirus (formerly respiratory syncytial virus [RSV]; family *Pneumoviridae*) has also been studied by cryo-ET and STA (Liljeroos et al., 2013). These virions display a wide range of morphologies including spherical and filamentous forms of different sizes. Interestingly a matrix layer of the M protein can only be seen sporadically in spherical particles but is common in the filamentous form. This M layer is thought to provide the membrane curvature required for budding. On the surface of the virion is the fusion protein F and the attachment glycoprotein G which both appear to be randomly distributed. The F protein can be seen in two different conformations, pre fusion and post-fusion, as determined by classification of subvolumes. This study notes that each virion typically has only one conformation of F protein on its surface but differences can be seen between virions. Another study goes further to suggest that the F protein is exclusively in the prefusion form on filamentous particles but in the post fusion form on spherical particles (Ke et al., 2018b). This suggests that the infectious form of the virus is the filamentous form and highlights the need for studying virions in their most native form, free from purification artefacts, that is by cryo-ET of budding sites on the cell surface (see section 5).

4. Envelope virus membrane fusion

4A. Fusion-triggered forms of purified virions

Entry of enveloped viruses into host cells can either occur by direct fusion at the plasma membrane or by endocytic pathways (i.e. macropinocytosis, clathrin-mediated and caveolin-mediated endocytosis), leading to the formation of endocytic vesicles and eventually fusion with endosomes or lysosomes (Yamauchi and Helenius, 2013). The harsh environment of

these compartments, including low pH and unusually high or low ionic concentration, often results in significant changes in the morphologies of the virions, particularly the envelope-displayed fusion proteins (Harrison, 2015).

Cryo-EM has become the principal technique to visualize the structural transitions that enveloped viruses and their fusion proteins undergo during fusion. Virions from different viral families have been imaged by cryo-EM in acidic conditions by changing the purified virions to low pH buffer. The results appear to agree that the fusion proteins in spite of their class (I, II, III), undergo varying degrees of structural changes. DENV virions with a bound Fab and incubated at pH 5.5 buffer have been used to reconstruct a cryo-EM map at 26 Å resolution (Zhang et al., 2015). This map revealed extended E-protein spikes with consistent shape to that of the E-protein trimer in its post fusion conformation solved by X-ray crystallography earlier (Modis et al., 2004). Averaging of side-views of the spikes at the edge of the virion allowed calculating 2D class averages of spikes (Zhang et al., 2015). As these experiments were carried out in the absence of target membranes, these results suggested that the observed trimer is a transient pre-fusion trimeric state of the E fusion protein, stabilised by the bound Fab (Zhang et al., 2015). Similar side-view averaging of BUNV GP spikes from the surface of the virions, imaged at low pH, has suggested that the GP lattice loses some of its contacts at the tips of the spikes mainly formed by the class II fusion GPs (Bowden et al., 2013). Likewise, 2D averages of TULV side views has demonstrated the collapse of its ordered tetrameric lattice under low pH conditions (Rissanen et al., 2017). A recent cryo-ET and STA investigation of the LASV GP spike complex supports the sensitivity of GP1 attachment glycoprotein towards ambient pH (Cohen-Dvashi et al., 2015; Li et al., 2016a; Pryce et al., 2019). Conformational differences can be observed for GP1 structure as the pH drops from neutral (8–7) to endosomal or lysosomal pH (6.5–3.0), ultimately resulting in the shedding of the GP1 and the fusogenic rearrangement of the GP2 fusion protein (Li et al., 2016a).

Not just low pH, but other factors, either physiological or non-physiological, can also be applied to trigger the fusion protein from its prefusion condition. HRPV5 is an enveloped archeal virus with a monomeric envelope fusion protein, which does not confer to any of the existing classes I–III (El Omari et al., 2019). HRPV5 virions have been triggered to their fusogenic conformation by exposure to high temperature (55^{o}C). This led to a conformational change in their monomeric fusion protein, allowing it to extend far enough to conceivably reach across the host cell S-layer to bridge the virion and host cell membranes (El Omari et al., 2019). Other factors such as the concentration of potassium ions (K^{+}) has also been shown to be crucial for fusion events. An STA study of HAZV GP has demonstrated that the Gc fusion protein can be triggered by high K^{+} concentration into an extended conformation and subsequently embedded into the target membrane of co-purified vesicles (Punch et al., 2018).

4B. Virus–liposome complexes

Liposomes have been used extensively as mimics of cellular plasma and endosomal membranes in cryo-EM studies of virus fusion. Liposomes serve as an accessible tool as their lipid compositions are well-defined and can be easily manipulated to suit the physiological fusion environment. As compared to a whole cell, the relatively small sizes of liposomes also enable cryo-EM imaging without complicated sample preparations such as

583 focused ion beam (FIB) milling or cryo-sectioning. The effect of various factors such as pH,
584 temperature, lipid composition, ion concentration, in addition to antibodies or fusion
585 inhibitors, have been investigated using virus–liposome complexes (Calder and Rosenthal,
586 2016)(Chlanda et al., 2016)(Halldorsson et al., 2018).
587
588 Visualization of influenza virus–liposome fusion events at low pH has been achieved with
589 cryo-ET and STA, showing a progression of sequential events from HA-liposome contact,
590 membrane–membrane contact, full fusion, to redistribution of viral components and contents
591 (Calder and Rosenthal, 2016). The M1 matrix layer has also been observed to undergo a
592 conformational change at low pH prior to dissociating from the viral membrane, allowing
593 membrane deformation and formation of a fusion pore (Fontana and Steven, 2013). In
594 corroboration with crystal structures of HA obtained at neutral (Wilson et al., 1981) and
595 fusion permissive pH (Bullough et al., 1994; Chen et al., 1999), cryo-EM investigations
596 (Calder et al., 2010) have established that HA (class I fusion protein) undergoes a
597 conformational change at low pH, exposing the fusion peptide for membrane fusion. Indeed,
598 cryo-EM snapshots and tomographic slices of influenza virus–liposome interactions at low
599 pH reveal an extended triple-stranded coiled coil HA structure, perpendicular to the
600 membrane, that can be seen inserted into the target membrane. The membranes are pulled
601 towards each other, first creating a dimple and then hemifusion of the two membranes. After
602 the eventual formation of the fusion pore the HA can be seen in the "foldback" conformation
603 radiating from the membrane contact points (Calder and Rosenthal, 2016). Another cryo-ET
604 study has proposed a hemifusion stalk-independent model of membrane fusion termed the
605 “rupture-insertion” pathway utilized when the cholesterol content in the liposomes is low
606 (Chlanda et al., 2016). Interestingly, the HA fusion peptide of influenza virus has been
607 observed to insert into the viral membrane in *cis* in the absence of a target membrane
608 (Calder et al., 2010; Ruigrok et al., 1986; Skehel et al., 1982)(Calder and Rosenthal, 2016).
609
610 A recent cryo-ET and STA study of RVFV Gc (class II fusion protein) (Halldorsson et al.,
611 2018) has shed more light on the prefusion conformation of Gc, how the hydrophobic fusion
612 peptide is protected prior to the fusion event and how the fusion loops are embedded in a
613 target membrane. Localized reconstructions of RVFV surface GP spikes have allowed their
614 structures to be resolved at sufficiently high resolution (~8 Å) for flexible fitting of Gn and Gc
615 X-ray crystallographic structures. This resulted in a model showing that the Gn glycoprotein
616 shields the fusion loop by associating noncovalently with the Gc glycoprotein in the pre-
617 fusion state at neutral pH (Halldorsson et al., 2018). Cryo-ET carried out at fusion permissive
618 low pH and in the presence of liposomes showed that the Gn-shield shifts away to expose
619 the fusion peptide, allowing extension of the Gc molecule from a kinked, likely metastable
620 conformation to a more straightened intermediate conformation. Extension of the Gc allows it
621 to embed its fusion loops in the target membrane, with the aromatic side chains projected
622 into the hydrophobic region of the lipid bilayer (Halldorsson et al., 2018). This Gn-fusion loop
623 shielding mechanism resembles that of alphaviruses CHIKV (Sun et al., 2013) and SFV
624 (Mancini et al., 2000), where the fusion peptide of the E1 fusion protein is shielded by the E2
625 receptor-binding protein but contrasts the homotypic shielding observed in E–E interactions
626 of the flaviviruses DENV (Kuhn et al., 2002; Zhang et al., 2003a) and ZIKV (Sirohi et al.,
627 2016).

5. Virus budding

Virus budding is a crucial step in the life cycle and propagation of enveloped viruses. Packaged with the newly synthesized genomic contents and viral proteins, virions escape from the host cell membrane prior to infecting more cells. Electron microscopy images show that budding virions can display different morphologies and often recruit viral matrix protein to the budding site. The assembly and organization of the matrix protein along with the spike GPs, NCs and in some cases also with the help of cellular ESCRT complexes induce a membrane curvature in the host cell membrane and form vesicles that are eventually pinched off to release the viral particles (Chen and Lamb, 2008). Other mechanisms that involve internal viral nonstructural proteins and lipid rafts have also been reported (Hyatt et al., 1993) (Ono and Freed, 2001)(Bavari et al., 2002)(Leser and Lamb, 2005). Cryo-ET of infected cells has been proven to be a useful technique to study the morphologically variable process of virion budding (Ke et al., 2018a)(Bharat et al., 2011)(Ke et al., 2018b)(Carlson et al., 2010).

The matrix protein (M) of MeV has been observed, using whole-cell cryo-ET and STA, to form a well-ordered lattice that lines the inner leaflet of the plasma or virion membrane of MeV-infected cells and released virus particles, respectively (Ke et al., 2018a). The M protein has also been shown to interact with the cytoplasmic or intravirionic tails of the envelope glycoproteins and the helical ribonucleoprotein (RNP) (Ke et al., 2018a). In contrast, purified MeV virions were observed to contain ~30 nm tubular structures composed of M protein tightly coating the inner RNP, but without M protein present at the membrane (Brown et al., 1987; Liljeroos et al., 2011). Matrix oligomerization at the membrane and association on the RNP suggest that the M protein plays essential role in MeV assembly and budding by coordinating the M–glycoprotein and M–RNP interactions and that this is likely a common assembly mechanism utilized across the *Paramyxoviridae* family. These observations suggest that the methods of virus preparation and purification may result in alterations of the virus particles and subsequently impact our interpretation and understanding of the data (Kiss et al., 2014).

The roles of matrix protein and NC in virus budding have also been studied in filoviruses such as MARV. Cryo-ET and STA investigations of intact MARV virions (Bharat et al., 2011) have revealed that the membrane-associated VP40 matrix protein interacts with other viral proteins such as VP24, VP35, and NC, and that NC displays a strong structural disparity with characteristic “pointed” and “barbed” ends by analogy with actin. The analysis of MARV-infected cells by cryo-ET has shown that the helical NCs associates laterally with the inner leaflet of the host plasma membrane and are subsequently enveloped to form filopodia-like membrane protrusions prior to excision, releasing filamentous particles. The virion VP40 lattice have been observed to undergo structural rearrangement when associated with NC as compared to VP40 in VLP without NC, indicating that the VP40-NC interaction is likely required for NC envelopment and budding. Interestingly, the filamentous rhabdovirus vesicular stomatitis virus (VSV), another member of *Mononegavirales*, appears to utilize different envelopment and budding mechanisms despite the morphological homology of its NC with that of filovirus (Ge et al., 2010). Evidently, the “barbed” ends of the VSV NC bud out first, whereas, all MARV NCs are oriented with their “pointed” ends outwards. This differential budding directionality, is however, reconciled by the authors as the requirement

for the first base of the genome (3') to be synthesized to bud first, placing the absolute RNA directionality a priority over the NC directionality.

A previous study of MARV budding has showed that filamentous particles constitute infectious virions while rounded particles of lower infectivity were released during late rounds of infection (Welsch et al., 2010). This morphological distinction has also been observed in the paramyxovirus RSV using cryo-ET in the presence of a fusion inhibitor to exclude the possibility of observing fusion events (Ke et al., 2018b). The particles are observed in various stages of the budding process including initiation, elongation, and scission. Interestingly, the particles bud in the filamentous form despite spherical forms of the virus have been also reported (Liljeroos et al., 2013). The authors suggest that this provides further evidence that the infectious form of RSV is the filamentous form.

In enveloped virions that lack a matrix protein, such as in the members of *Bunyavirales*, organization of the spike GPs may become a key contributor to viral budding. For example, hantavirus TULV tetrameric GP forms locally ordered patches as shown by cryo-ET and STA. These patches have been proposed to create membrane curvature and contribute to the budding of hantaviruses (Huiskonen et al., 2010). Interestingly, nairovirus HAZV GP has also been observed to arrange in ordered tetrameric patches (Punch et al., 2018). Analogously, locally ordered patches of GP trimers have been observed also in BUNV, an orthobunyavirus, suggesting that such local order may be a generic driver of budding in pleomorphic bunyavirus virions (Bowden et al., 2013).

For retroviruses, the Gag polyprotein mediates many essential events including membrane binding, virion assembly, and genome packaging. Cryo-ET and STA analysis of native HIV-1 budding sites revealed a consistently continuous lattice of Gag polyprotein with the same organization and structure as seen in released immature virions, indicative that the organization of these particles is determined at their intracellular assembly point (Carlson et al., 2010). Cortical actin filaments were also visualized at these sites, particularly the filopodia-assisted buds, suggesting a role of actin filaments in retrovirus assembly. A lattice lacking the NC-RNA-p6 complex was also observed in some budding sites and virions, indicating that the viral genome was absent, an observation attributed to premature proteolytic maturation and failure to recruit the ESCRT machinery in some HIV-1 infected T-cells. Interestingly, the use of whole-cell cryo-ET permitted the direct visualizations of HIV-1 virions and VLPs connected to each other and to the plasma membrane by highly dynamic and filamentous proteinaceous bodies, referred as tethers (Strauss et al., 2016). The localization of tethers at budding sites supported an established restriction model for HIV-1 release and dissemination. Indeed, observation of beads-on-a-string appearance on tomographic images suggested that virion budding had occurred sequentially through a tetherin-enriched microdomain.

6. Neutralisation

The increasing number of outbreaks caused by arboviruses, such as DENV, ZIKV and CHIKV, has placed tremendous pressure on scientists worldwide to generate therapeutic agents or vaccines in response to the epidemics (Weaver et al., 2018). Cryo-EM has been applied extensively to study the structures of virion–antibody complexes which have

provided insights into the molecular basis of antibody-mediated neutralisation mechanisms and the identification of potential therapeutic immunogens.

The cryo-EM structures of DENV in complex with monoclonal antibodies (mAb) at elevated temperatures have provided a wealth of detailed information into neutralization of different DENV serotypes. These structures show that the bumpy form of DENV2 is able to bind an anti-DENV Fab 1A1D-2 (Lok et al., 2008) and E104 (Zhang et al., 2015) only at elevated temperatures. The cryo-EM structure of Fab 1A1D–DENV2 complex demonstrates that the complex formation was temperature dependent with a higher level of Fab binding at 37^{o}C than at ambient temperature due to the exposure of a hidden part of the Fab binding epitope on the E proteins (Lok et al., 2008). However, it has also been shown that this temperature-dependent transition from smooth to bumpy is strain-dependent. The cryo-EM structure of the DENV4 virion at 4.1-Å resolution suggests that this serotype has higher thermal stability than other DENV strains (Kostyuchenko et al., 2014). Furthermore, unlike other DENV strains, these virions do not expose the fusion loops to allow binding to flavivirus mAbs until the temperature is increased to 40^{o}C (Sukupolvi-Petty et al., 2013). A DENV2-specific human mAb (2D22) complex cryo-EM structure suggests that HMAb 2D22 neutralises DENV2 by binding E dimers and prevents the E protein rearrangement required for viral entry (Fibriansah et al., 2015a). The cryo-EM structure of Fab HMAb 5J7-DENV3 complex shows that a single Fab molecule of HMAb 5J7 simultaneously binds to three functionally significant E protein domains, each on a different E protein molecule, to prevent virus attachment (Fibriansah et al., 2015b). The cryo-EM structure of a DENV1–HMAb 1F4 complex has revealed that the HMAb 1F4 binds to DI and DI–DII hinge region on an E protein monomer to prevent different stages of viral entry (Fibriansah et al., 2014) while the DENV1 specific HM14c10 targets an adjacent surface of E protein dimers to neutralise the virus by blocking virus attachment as shown by cryo-EM of the DENV1–HMAb 14c10 complex (Teoh et al., 2012). More recently, cryo-EM has been applied to study two highly neutralising antibodies (2C8 and 3H5) against DENV E protein and to understand the difference in their capacity to promote antibody dependent enhancement (ADE) (Renner et al., 2018; Wirawan et al., 2018). It was proposed that antibody 3H5 promoted minimal ADE by its unusual binding to the viral surface resulting in poor access to Fc region. Another study looked at the role of anti-prM antibodies in the pathogenesis of immature DENV by the cryo-EM structures of the immature DENV in complex with a Fag fragment of HMAb 1H10, at different pH values. This suggested the mechanism by which the Fab 1H10 enhanced attachment of immature DENV to liposomes by increasing dissociation of prM from E (Wirawan et al., 2018).

Recent epidemics of ZIKV in the Americas have accelerated structural studies into the neutralization mechanism of ZIKV virion–mAb complexes (Cauchemez et al., 2016; Fauci and Morens, 2016; Mlakar et al., 2016). The first cryo-EM structure of a ZIKV–mAb complex used a cross-reactive DENV mAb (C10) which inhibited viral fusion to acidified endosomes by locking of the E proteins (Zhang et al., 2016). This was followed by the 9-Å resolution cryo-EM complex structure of ZIKV and the ZIKV specific human mAb (Fab Z23) which demonstrated the binding of Fab Z23 to DIII domain of the E protein (Wang et al., 2016b). Another study showed that the neutralising human mAb (ZIKV-117) cross-links monomers with E dimers as well as between neighbouring E dimers to prevent the conformational changes of E dimers into fusogenic trimers in acidified endosomes (Hasan et al., 2017). More recently, a 4-Å resolution cryo-EM structure of ZIKV in complex with Fab fragments of

the highly specific human mAb (ZIKV-195) suggested that Fab ZIKV-195 neutralises ZIKV by binding to two adjacent E dimers to prevent the structural reorganization to trimers required for membrane fusion (Long et al., 2019). Cryo-EM has been applied also on other flavivirus–mAb complexes. TBEV, in complex with the neutralising mouse mAb Fab fragment (19/1786) has been resolved to a resolution of 3.9 Å revealing that this Fab neutralises by inhibiting virus-induced membrane fusion (Füzik et al., 2018). The 14.5 Å resolution cryo-EM structure of WNV in complex with the Fab of the strongly neutralizing antibody E16 has revealed that it binds to DIII and neutralises by preventing the conformational change of E prior to membrane fusion (Kaufmann et al., 2006).

Many alphavirus neutralizing antibodies in complex with virions have been studied by cryo-EM. These studies have shown that most of these neutralizing mAbs target the exposed E2 protein cap (Long et al., 2015; Sun et al., 2013) (Porta et al., 2016) (Fox et al., 2015) (Hasan et al., 2018b). One of the first studies produced four ~15-Å resolution cryo-EM structures of CHIKV VLPs complexed with the Fab fragments of neutralizing mouse MAbs (Sun et al., 2013). This study shows that the CHK-152 mAb neutralises by stabilising the viral surface and preventing the exposure of fusion-loop and thereby the fusion. The three mAbs CHK-9, m10 and m242 antibodies have been suggested to block the receptor-attachment site (Sun et al., 2013). More recently, two cryo-EM studies of CHIKV VLPs complexed with Fabs of highly neutralizing human mAbs have been described providing insights into the structural basis of neutralisation (Long et al., 2015; Porta et al., 2016). Furthermore, it has been suggested that the Fabs 4J21 and 5M16 bind to domains B on E2 blocking virus fusion (Long et al., 2015). The Fab 8B10 inhibits attachment by covering the receptor binding site whereas 5F10 inhibits fusion by restricting B domain movement (Porta et al., 2016). Another cryo-EM study of Fab fragments of two human mAbs has revealed a mechanism for inhibiting membrane fusion and also identified E2-W64 as a key neutralizing epitope of CHIKV E protein (Jin et al., 2015). The 16-Å resolution cryo-EM structure of CHIKV in complex with CHK-265 Fab fragments has shown that the Fab binds to domain B of E2 and induces significant conformational changes in domain A and cross-links adjacent E2 spikes to block viral entry and egress steps (Fox et al., 2015). The cryo-EM study of another alphavirus, VEEV, in complex with the highly neutralizing mAb Fab fragments (F5 and 3B4C-4) at resolution of ~17.5 Å has revealed the difference in their neutralisation mechanisms. While both Fab fragments neutralise by stabilising E2 trimeric spikes and preventing the viral fusion, the F5 cross-links E2 within a trimeric spike to block the receptor binding site whereas the 3B4C-4 Fab cross links E2 from neighbouring spikes to prevent the exposure of the fusion loop by steric hindrance (Porta et al., 2014). Recent cryo-EM studies looking at the SINV-EEEV chimera in complex with 5 different Fabs have revealed that three Fab fragments of neutralizing mAbs (EEEV-5, EEEV-42 and EEEV-58) bound to domain A of E2 protein which cause intraspike cross-linking while the other two (EEEV-3 and EEEV-69) interact only with domain B favouring interspike cross-linking (Hasan et al., 2018b).

In addition to extensive cryo-EM studies of the arboviruses belonging to *Flaviviridae* and *Togaviridae* families described above, cryo-EM has been applied to study the structures of virion–antibody complexes for several viruses from other families, notably HIV and EBOV. STA has been used to study the HIV Env trimer on native virions in complex with a broadly neutralising antibody Fab fragment, b12, and the cell surface receptor, CD4 (Liu et al., 2008). This study shows that both the Fab and the receptor cause a large conformational change that “opens” the trimer but this change is more dramatic with the receptor CD4. It

has therefore been proposed that the b12 antibody exerts its neutralisating effect by locking Env in a confirmation that prevents a further CD4 induced conformational change that is required to continue the virus life cycle. To understand the structural basis of ZMapp (a cocktail of 3 mAbs: c24G4, c4G7 and C13C6), a promising anti-EBOV therapeutic, cryo-EM structures of c2G4, c4G7 and c13C6 IgGs bound to EBOV VLPs have been studied by STA (Tran et al., 2016). This study suggests that two of these antibodies (c2G4 and c4G7) remain bound through the endocytic pathway and exert their neutralising effect by preventing conformational changes required for fusion.

7. Conclusions

Cryo-EM has always been the method of choice to study the structures of enveloped virions. Due to technological developments in both microscope hardware and image processing software, the rate of discoveries has been accelerating in the past five years. Structures of regular enveloped virions whose protein shell(s) follow icosahedral symmetry can now be determined in a matter of days by SPA. Pleomorphic virions and virions in complex with receptors or antibodies remain a challenge for structure determination. Those virions or complexes that show slight deviations from perfect icosahedral symmetry may be tractable by improved computational 2D averaging approaches that deal with structural deformations accurately. When deviations are more severe or when the virion structure is truly pleomorphic or filamentous, STA remains the method of choice and is becoming more widely utilized. In near future more studies are expected to utilize various hybrid data processing approaches to tackle the most challenging targets for which resolution has remained limited or which have remained entirely unattainable. The 2D and 3D averaging workflows depicted in Figure 2 will likely merge into one framework within the same software package in the future. This should facilitate routinely resolving structural components in pleomorphic, enveloped virions to near-atomic resolution and further to address mechanisms of virus infection and neutralization in enveloped viruses in general.

Tables

Table 1. Examples of enveloped virion structures and their membrane associated components determined by different cryogenic electron microscopy data processing strategies.

Virus	Compo-nent	Method and steps*	Reso-lution (Å)	Accession codes	Reference
Simian immunodeficiency virus 1 (*Retroviridae*)	Capsomer (Env)	3D 1-2-4	28	EMD-1216 PDB:2BF1	(Zanetti et al., 2006)
Zika virus (*Flaviviridae*)	Virion	2D 1-2	3.1	EMD-7543 PDB:6CO8	(Sevvana et al., 2018)
Sindbis virus (*Togaviridae*)	Virion	2D 1-2-3-4-5	3.5	EMD-9693 PDB:6IMM	(Chen et al., 2018)
Rift Valley fever virus (*Phenuiviridae*)	Capsomer (Gn–Gc)	2D 1-2-3-4	7.7	EMD-4201 PDB:6F9F	(Halldorsson et al., 2018)
Hantaan virus (*Hantaviridae*)	Capsomer (Gn–Gc)	2D 1-2'-4	25	N/A	(Battisti et al., 2011)
Tula virus (*Hantaviridae*)	Capsomer (Gn–Gc)	3D 1-2-4	16	EMD-3364	(Li et al., 2016b)
Bunyamwera virus (*Orthobunyaviridae*)	Capsomer (Gn–Gc)	3D 1-2-4	30	EMD-2352	(Bowden et al., 2013)
Hazara virus (*Nairoviridae*)	Capsomer (Gn–Gc)	3D 1-2-4	25	N/A	(Punch et al., 2018)
Lassa virus (*Arenaviridae*)	Capsomer (GP1–GP2)	3D 1-2-4	14.0	EMD-3290	(Li et al., 2016a)
Measles virus (*Paramyxoviridae*)	Virion	3D 1	N/A	N/A	(Ke et al., 2018a)
Ebola virus (*Filoviridae*)	Capsomer (GP)	2D 1-2	11	EMD-8036	(Beniac and Booth, 2017)
Influenza virus A (*Orthomyxoviridae*)	Virion	3D 1	N/A	N/A	(Calder et al., 2010)
Haloarcula hispanica SH1 virus (*Sphaerolipoviridae*)	Virion	2D 1-2-3-4-5	3.8	EMD-4633 PDB:6QT9	(de Colibus et al., 2019)

* The steps refer to different parts of the various image processing workflows in Figure 2. For steps in 2D workflows (single particle averaging and sub-particle averaging), refer to Figure 2A. For steps in 3D workflows (tomography and sub-tomogram averaging), refer to Figure 2B.

References

Abrescia, N.G.A., Cockburn, J.J.B., Grimes, J.M., Sutton, G.C., Diprose, J.M., Butcher, S.J., Fuller, S.D., San Martín, C., Burnett, R.M., Stuart, D.I., et al. (2004). Insights into assembly from structural analysis of bacteriophage PRD1. Nature *432*, 68–74.

Abrescia, N.G.A., Grimes, J.M., Kivelä, H.M., Assenberg, R., Sutton, G.C., Butcher, S.J., Bamford, J.K.H., Bamford, D.H., and Stuart, D.I. (2008). Insights into virus evolution and membrane biogenesis from the structure of the marine lipid-containing bacteriophage PM2. Mol. Cell *31*, 749–761.

Allison, S.L., Schalich, J., Stiasny, K., Mandl, C.W., Kunz, C., and Heinz, F.X. (1995). Oligomeric rearrangement of tick-borne encephalitis virus envelope proteins induced by an acidic pH. J. Virol. *69*, 695–700.

Bai, X.-C., Rajendra, E., Yang, G., Shi, Y., and Scheres, S.H. (2015). Sampling the conformational space of the catalytic subunit of human γ-secretase. Elife *4*.

Battisti, A.J., -K. Chu, Y., Chipman, P.R., Kaufmann, B., Jonsson, C.B., and Rossmann, M.G. (2010). Structural Studies of Hantaan Virus. J. Virol. *85*, 835–841.

Battisti, A.J., Chu, Y.-K., Chipman, P.R., Kaufmann, B., Jonsson, C.B., and Rossmann, M.G. (2011). Structural studies of Hantaan virus. J. Virol. *85*, 835–841.

Battisti, A.J., Meng, G., Winkler, D.C., McGinnes, L.W., Plevka, P., Steven, A.C., Morrison, T.G., and Rossmann, M.G. (2012). Structure and assembly of a paramyxovirus matrix protein. Proc. Natl. Acad. Sci. U. S. A. *109*, 13996–14000.

Bavari, S., Bosio, C.M., Wiegand, E., Ruthel, G., Will, A.B., Geisbert, T.W., Hevey, M., Schmaljohn, C., Schmaljohn, A., and Aman, M.J. (2002). Lipid raft microdomains: a gateway for compartmentalized trafficking of Ebola and Marburg viruses. J. Exp. Med. *195*, 593–602.

Bederka, L.H., Bonhomme, C.J., Ling, E.L., and Buchmeier, M.J. (2014). Arenavirus stable signal peptide is the keystone subunit for glycoprotein complex organization. MBio *5*, e02063.

Beniac, D.R., and Booth, T.F. (2017). Structure of the Ebola virus glycoprotein spike within the virion envelope at 11 Å resolution. Sci. Rep. *7*, 46374.

Bharat, T.A.M., Riches, J.D., Kolesnikova, L., Welsch, S., Krähling, V., Davey, N., Parsy, M.-L., Becker, S., and Briggs, J.A.G. (2011). Cryo-electron tomography of Marburg virus particles and their morphogenesis within infected cells. PLoS Biol. *9*, e1001196.

Bharat, T.A.M., Noda, T., Riches, J.D., Kraehling, V., Kolesnikova, L., Becker, S., Kawaoka, Y., and Briggs, J.A.G. (2012). Structural dissection of Ebola virus and its assembly determinants using cryo-electron tomography. Proc. Natl. Acad. Sci. U. S. A. *109*, 4275–4280.

Bowden, T.A., Bitto, D., McLees, A., Yeromonahos, C., Elliott, R.M., and Huiskonen, J.T. (2013). Orthobunyavirus ultrastructure and the curious tripodal glycoprotein spike. PLoS Pathog. *9*, e1003374.

Bressanelli, S., Stiasny, K., Allison, S.L., Stura, E.A., Duquerroy, S., Lescar, J., Heinz, F.X., and Rey, F.A. (2004). Structure of a flavivirus envelope glycoprotein in its low-pH-induced membrane fusion conformation. EMBO J. *23*, 728–738.

Briggs, J.A.G., Wilk, T., Welker, R., Kräusslich, H.-G., and Fuller, S.D. (2003). Structural organization of authentic, mature HIV-1 virions and cores. EMBO J. *22*, 1707–1715.

Briggs, J.A.G., Grünewald, K., Glass, B., Förster, F., Kräusslich, H.-G., and Fuller, S.D. (2006). The mechanism of HIV-1 core assembly: insights from three-dimensional reconstructions of authentic virions. Structure *14*, 15–20.

Brown, H.R., Goller, N., Thormar, H., and Norrby, E. (1987). Fuzzy material surrounding measles virus nucleocapsids identified as matrix protein. Brief report. Arch. Virol. *94*, 163–168.

Bullough, P.A., Hughson, F.M., Skehel, J.J., and Wiley, D.C. (1994). Structure of influenza haemagglutinin at the pH of membrane fusion. Nature *371*, 37–43.

Calder, L.J., and Rosenthal, P.B. (2016). Cryomicroscopy provides structural snapshots of influenza virus membrane fusion. Nat. Struct. Mol. Biol. *23*, 853–858.

Calder, L.J., Wasilewski, S., Berriman, J.A., and Rosenthal, P.B. (2010). Structural organization of a filamentous influenza A virus. Proc. Natl. Acad. Sci. U. S. A. *107*, 10685–10690.

Carlson, L.-A., de Marco, A., Oberwinkler, H., Habermann, A., Briggs, J.A.G., Kräusslich, H.-G., and Grünewald, K. (2010). Cryo electron tomography of native HIV-1 budding sites. PLoS Pathog. *6*, e1001173.

Castaño-Díez, D., Kudryashev, M., and Stahlberg, H. (2017). Dynamo Catalogue: Geometrical tools and data management for particle picking in subtomogram averaging of cryo-electron tomograms. J. Struct. Biol. *197*, 135–144.

Cauchemez, S., Besnard, M., Bompard, P., Dub, T., Guillemette-Artur, P., Eyrolle-Guignot, D., Salje, H., Van Kerkhove, M.D., Abadie, V., Garel, C., et al. (2016). Association between Zika virus and microcephaly in French Polynesia, 2013–15: a retrospective study. The Lancet *387*, 2125–2132.

Chen, B.J., and Lamb, R.A. (2008). Mechanisms for enveloped virus budding: can some viruses do without an ESCRT? Virology *372*, 221–232.

Chen, J., Skehel, J.J., and Wiley, D.C. (1999). N- and C-terminal residues combine in the fusion-pH influenza hemagglutinin HA(2) subunit to form an N cap that terminates the triple-stranded coiled coil. Proc. Natl. Acad. Sci. U. S. A. *96*, 8967–8972.

Chen, L., Wang, M., Zhu, D., Sun, Z., Ma, J., Wang, J., Kong, L., Wang, S., Liu, Z., Wei, L., et al. (2018). Implication for alphavirus host-cell entry and assembly indicated by a 3.5Å resolution cryo-EM structure. Nat. Commun. *9*, 5326.

Chlanda, P., Mekhedov, E., Waters, H., Schwartz, C.L., Fischer, E.R., Ryham, R.J., Cohen, F.S., Blank, P.S., and Zimmerberg, J. (2016). The hemifusion structure induced by influenza virus haemagglutinin is determined by physical properties of the target membranes. Nat Microbiol *1*, 16050.

Cohen-Dvashi, H., Cohen, N., Israeli, H., and Diskin, R. (2015). Molecular Mechanism for LAMP1 Recognition by Lassa Virus. J. Virol. *89*, 7584–7592.

Cyrklaff, M., Risco, C., Fernández, J.J., Jiménez, M.V., Estéban, M., Baumeister, W., and Carrascosa, J.L. (2005). Cryo-electron tomography of vaccinia virus. Proc. Natl. Acad. Sci. U. S. A. *102*, 2772–2777.

935 Dryden, K.A., Wieland, S.F., Whitten-Bauer, C., Gerin, J.L., Chisari, F.V., and Yeager, M.
936 (2006). Native hepatitis B virions and capsids visualized by electron cryomicroscopy. Mol.
937 Cell *22*, 843–850.

938 Effantin, G., Estrozi, L.F., Aschman, N., Renesto, P., Stanke, N., Lindemann, D., Schoehn,
939 G., and Weissenhorn, W. (2016). Cryo-electron Microscopy Structure of the Native Prototype
940 Foamy Virus Glycoprotein and Virus Architecture. PLoS Pathog. *12*, e1005721.

941 El Omari, K., Li, S., Kotecha, A., Walter, T.S., Bignon, E.A., Harlos, K., Somerharju, P., De
942 Haas, F., Clare, D.K., Molin, M., et al. (2019). The structure of a prokaryotic viral envelope
943 protein expands the landscape of membrane fusion proteins. Nat. Commun. *10*, 846.

944 Fauci, A.S., and Morens, D.M. (2016). Zika Virus in the Americas--Yet Another Arbovirus
945 Threat. N. Engl. J. Med. *374*, 601–604.

946 Fibriansah, G., Ng, T.-S., Kostyuchenko, V.A., Lee, J., Lee, S., Wang, J., and Lok, S.-M.
947 (2013). Structural changes in dengue virus when exposed to a temperature of 37°C. J. Virol.
948 *87*, 7585–7592.

949 Fibriansah, G., Tan, J.L., Smith, S.A., de Alwis, A.R., Ng, T.-S., Kostyuchenko, V.A., Ibarra,
950 K.D., Wang, J., Harris, E., de Silva, A., et al. (2014). A potent anti-dengue human antibody
951 preferentially recognizes the conformation of E protein monomers assembled on the virus
952 surface. EMBO Mol. Med. *6*, 358–371.

953 Fibriansah, G., Ibarra, K.D., Ng, T.-S., Smith, S.A., Tan, J.L., Lim, X.-N., Ooi, J.S.G.,
954 Kostyuchenko, V.A., Wang, J., de Silva, A.M., et al. (2015a). DENGUE VIRUS. Cryo-EM
955 structure of an antibody that neutralizes dengue virus type 2 by locking E protein dimers.
956 Science *349*, 88–91.

957 Fibriansah, G., Tan, J.L., Smith, S.A., de Alwis, R., Ng, T.-S., Kostyuchenko, V.A., Jadi,
958 R.S., Kukkaro, P., de Silva, A.M., Crowe, J.E., et al. (2015b). A highly potent human
959 antibody neutralizes dengue virus serotype 3 by binding across three surface proteins. Nat.
960 Commun. *6*, 6341.

961 Fontana, J., and Steven, A.C. (2013). At low pH, influenza virus matrix protein M1
962 undergoes a conformational change prior to dissociating from the membrane. J. Virol. *87*,
963 5621–5628.

964 Förster, F., Medalia, O., Zauberman, N., Baumeister, W., and Fass, D. (2005). Retrovirus
965 envelope protein complex structure in situ studied by cryo-electron tomography. Proc. Natl.
966 Acad. Sci. U. S. A. *102*, 4729–4734.

967 Fox, J.M., Long, F., Edeling, M.A., Lin, H., van Duijl-Richter, M.K.S., Fong, R.H., Kahle,
968 K.M., Smit, J.M., Jin, J., Simmons, G., et al. (2015). Broadly Neutralizing Alphavirus
969 Antibodies Bind an Epitope on E2 and Inhibit Entry and Egress. Cell *163*, 1095–1107.

970 Fuller, S.D., Berriman, J.A., Butcher, S.J., and Gowen, B.E. (1995). Low pH induces
971 swiveling of the glycoprotein heterodimers in the Semliki forest virus spike complex. Cell *81*,
972 715–725.

973 Füzik, T., Formanová, P., Růžek, D., Yoshii, K., Niedrig, M., and Plevka, P. (2018). Structure
974 of tick-borne encephalitis virus and its neutralization by a monoclonal antibody. Nat.
975 Commun. *9*, 436.

976 Ge, P., Tsao, J., Schein, S., Green, T.J., Luo, M., and Zhou, Z.H. (2010). Cryo-EM model of
977 the bullet-shaped vesicular stomatitis virus. Science *327*, 689–693.

978 Grunewald, K. (2003). Three-Dimensional Structure of Herpes Simplex Virus from Cryo-
979 Electron Tomography. Science *302*, 1396–1398.

980 Gui, L., Jurgens, E.M., Ebner, J.L., Porotto, M., Moscona, A., and Lee, K.K. (2015). Electron
981 tomography imaging of surface glycoproteins on human parainfluenza virus 3: association of
982 receptor binding and fusion proteins before receptor engagement. MBio *6*, e02393–14.

983 Guichard, P., Krell, T., Chevalier, M., Vaysse, C., Adam, O., Ronzon, F., and Marco, S.
984 (2011). Three dimensional morphology of rabies virus studied by cryo-electron tomography.
985 J. Struct. Biol. *176*, 32–40.

986 Halldorsson, S., Li, S., Li, M., Harlos, K., Bowden, T.A., and Huiskonen, J.T. (2018).
987 Shielding and activation of a viral membrane fusion protein. Nat. Commun. *9*, 349.

988 Happonen, L.J., Redder, P., Peng, X., Reigstad, L.J., Prangishvili, D., and Butcher, S.J.
989 (2010). Familial relationships in hyperthermo- and acidophilic archaeal viruses. J. Virol. *84*,
990 4747–4754.

991 Harris, A., Cardone, G., Winkler, D.C., Heymann, J.B., Brecher, M., White, J.M., and Steven,
992 A.C. (2006). Influenza virus pleiomorphy characterized by cryoelectron tomography. Proc.
993 Natl. Acad. Sci. U. S. A. *103*, 19123–19127.

994 Harrison, S.C. (2015). Viral membrane fusion. Virology *479-480*, 498–507.

995 Hasan, S.S., Saif Hasan, S., Miller, A., Sapparapu, G., Fernandez, E., Klose, T., Long, F.,
996 Fokine, A., Porta, J.C., Jiang, W., et al. (2017). A human antibody against Zika virus
997 crosslinks the E protein to prevent infection. Nat. Commun. *8*, 14722.

998 Hasan, S.S., Sevvana, M., Kuhn, R.J., and Rossmann, M.G. (2018a). Structural biology of
999 Zika virus and other flaviviruses. Nat. Struct. Mol. Biol. *25*, 13–20.

1000 Hasan, S.S., Sun, C., Kim, A.S., Watanabe, Y., Chen, C.-L., Klose, T., Buda, G., Crispin, M.,
1001 Diamond, M.S., Klimstra, W.B., et al. (2018b). Cryo-EM Structures of Eastern Equine
1002 Encephalitis Virus Reveal Mechanisms of Virus Disassembly and Antibody Neutralization.
1003 Cell Rep. *25*, 3136–3147.e5.

1004 Hastie, K.M., Zandonatti, M.A., Kleinfelter, L.M., Heinrich, M.L., Rowland, M.M., Chandran,
1005 K., Branco, L.M., Robinson, J.E., Garry, R.F., and Saphire, E.O. (2017). Structural basis for
1006 antibody-mediated neutralization of Lassa virus. Science *356*, 923–928.

1007 Hetzel, U., Sironen, T., Laurinmäki, P., Liljeroos, L., Patjas, A., Henttonen, H., Vaheri, A.,
1008 Artelt, A., Kipar, A., Butcher, S.J., et al. (2013). Isolation, identification, and characterization
1009 of novel arenaviruses, the etiological agents of boid inclusion body disease. J. Virol. *87*,
1010 10918–10935.

1011 Huiskonen, J.T. (2018). Image processing for cryogenic transmission electron microscopy of
1012 symmetry-mismatched complexes. Biosci. Rep.

1013 Huiskonen, J.T., Kivelä, H.M., Bamford, D.H., and Butcher, S.J. (2004). The PM2 virion has
1014 a novel organization with an internal membrane and pentameric receptor binding spikes.
1015 Nat. Struct. Mol. Biol. *11*, 850–856.

1016 Huiskonen, J.T., Jäälinoja, H.T., Briggs, J.A.G., Fuller, S.D., and Butcher, S.J. (2007).
1017 Structure of a hexameric RNA packaging motor in a viral polymerase complex. J. Struct.
1018 Biol. *158*, 156–164.

1019 Huiskonen, J.T., Overby, A.K., Weber, F., and Grünewald, K. (2009). Electron cryo-

microscopy and single-particle averaging of Rift Valley fever virus: evidence for GN-GC glycoprotein heterodimers. J. Virol. *83*, 3762–3769.

Huiskonen, J.T., Hepojoki, J., Laurinmäki, P., Vaheri, A., Lankinen, H., Butcher, S.J., and Grünewald, K. (2010). Electron cryotomography of Tula hantavirus suggests a unique assembly paradigm for enveloped viruses. J. Virol. *84*, 4889–4897.

Huiskonen, J.T., Parsy, M.-L., Li, S., Bitto, D., Renner, M., and Bowden, T.A. (2014). Averaging of viral envelope glycoprotein spikes from electron cryotomography reconstructions using Jsubtomo. J. Vis. Exp. e51714.

Hyatt, A.D., Zhao, Y., and Roy, P. (1993). Release of bluetongue virus-like particles from insect cells is mediated by BTV nonstructural protein NS3/NS3A. Virology *193*, 592–603.

Ilca, S.L., Kotecha, A., Sun, X., Poranen, M.M., Stuart, D.I., and Huiskonen, J.T. (2015). Localized reconstruction of subunits from electron cryomicroscopy images of macromolecular complexes. Nat. Commun. *6*, 8843.

Jäälinoja, H.T., Huiskonen, J.T., and Butcher, S.J. (2007a). Electron cryomicroscopy comparison of the architectures of the enveloped bacteriophages phi6 and phi8. Structure *15*, 157–167.

Jäälinoja, H.T., Huiskonen, J.T., and Butcher, S.J. (2007b). Electron Cryomicroscopy Comparison of the Architectures of the Enveloped Bacteriophages ϕ6 and ϕ8. Structure *15*, 157–167.

Jin, J., Liss, N.M., Chen, D.-H., Liao, M., Fox, J.M., Shimak, R.M., Fong, R.H., Chafets, D., Bakkour, S., Keating, S., et al. (2015). Neutralizing Monoclonal Antibodies Block Chikungunya Virus Entry and Release by Targeting an Epitope Critical to Viral Pathogenesis. Cell Rep. *13*, 2553–2564.

Kaufmann, B., Nybakken, G.E., Chipman, P.R., Zhang, W., Diamond, M.S., Fremont, D.H., Kuhn, R.J., and Rossmann, M.G. (2006). West Nile virus in complex with the Fab fragment of a neutralizing monoclonal antibody. Proc. Natl. Acad. Sci. U. S. A. *103*, 12400–12404.

Ke, Z., Strauss, J.D., Hampton, C.M., Brindley, M.A., Dillard, R.S., Leon, F., Lamb, K.M., Plemper, R.K., and Wright, E.R. (2018a). Promotion of virus assembly and organization by the measles virus matrix protein. Nat. Commun. *9*, 1736.

Ke, Z., Dillard, R.S., Chirkova, T., Leon, F., Stobart, C.C., Hampton, C.M., Strauss, J.D., Rajan, D., Rostad, C.A., Taylor, J.V., et al. (2018b). The Morphology and Assembly of Respiratory Syncytial Virus Revealed by Cryo-Electron Tomography. Viruses *10*.

Khayat, R., Fu, C.-Y., Ortmann, A.C., Young, M.J., and Johnson, J.E. (2010). The architecture and chemical stability of the archaeal Sulfolobus turreted icosahedral virus. J. Virol. *84*, 9575–9583.

Kielian, M. (2014). Mechanisms of Virus Membrane Fusion Proteins. Annu Rev Virol *1*, 171–189.

Kiss, G., Chen, X., Brindley, M.A., Campbell, P., Afonso, C.L., Ke, Z., Holl, J.M., Guerrero-Ferreira, R.C., Byrd-Leotis, L.A., Steel, J., et al. (2014). Capturing enveloped viruses on affinity grids for downstream cryo-electron microscopy applications. Microsc. Microanal. *20*, 164–174.

Klose, T., Kuznetsov, Y.G., Xiao, C., Sun, S., McPherson, A., and Rossmann, M.G. (2010).

1062 The three-dimensional structure of Mimivirus. Intervirology *53*, 268–273.

1063 Kostyuchenko, V.A., Chew, P.L., Ng, T.-S., and Lok, S.-M. (2014). Near-atomic resolution
1064 cryo-electron microscopic structure of dengue serotype 4 virus. J. Virol. *88*, 477–482.

1065 Kostyuchenko, V.A., Lim, E.X.Y., Zhang, S., Fibriansah, G., Ng, T.-S., Ooi, J.S.G., Shi, J.,
1066 and Lok, S.-M. (2016). Structure of the thermally stable Zika virus. Nature *533*, 425–428.

1067 Kühlbrandt, W. (2014). Biochemistry. The resolution revolution. Science *343*, 1443–1444.

1068 Kuhn, R.J., Zhang, W., Rossmann, M.G., Pletnev, S.V., Corver, J., Lenches, E., Jones, C.T.,
1069 Mukhopadhyay, S., Chipman, P.R., Strauss, E.G., et al. (2002). Structure of dengue virus:
1070 implications for flavivirus organization, maturation, and fusion. Cell *108*, 717–725.

1071 Laanto, E., Mäntynen, S., De Colibus, L., Marjakangas, J., Gillum, A., Stuart, D.I., Ravantti,
1072 J.J., Huiskonen, J.T., and Sundberg, L.-R. (2017). Virus found in a boreal lake links ssDNA
1073 and dsDNA viruses. Proceedings of the National Academy of Sciences *114*, 8378–8383.

1074 Laurinmäki, P.A., Huiskonen, J.T., Bamford, D.H., and Butcher, S.J. (2005). Membrane
1075 proteins modulate the bilayer curvature in the bacterial virus Bam35. Structure *13*, 1819–
1076 1828.

1077 Leser, G.P., and Lamb, R.A. (2005). Influenza virus assembly and budding in raft-derived
1078 microdomains: a quantitative analysis of the surface distribution of HA, NA and M2 proteins.
1079 Virology *342*, 215–227.

1080 Li, S., Sun, Z., Pryce, R., Parsy, M.-L., Fehling, S.K., Schlie, K., Siebert, C.A., Garten, W.,
1081 Bowden, T.A., Strecker, T., et al. (2016a). Acidic pH-Induced Conformations and LAMP1
1082 Binding of the Lassa Virus Glycoprotein Spike. PLoS Pathog. *12*, e1005418.

1083 Li, S., Rissanen, I., Zeltina, A., Hepojoki, J., Raghwani, J., Harlos, K., Pybus, O.G.,
1084 Huiskonen, J.T., and Bowden, T.A. (2016b). A Molecular-Level Account of the Antigenic
1085 Hantaviral Surface. Cell Rep. *15*, 959–967.

1086 Liljeroos, L., Huiskonen, J.T., Ora, A., Susi, P., and Butcher, S.J. (2011). Electron
1087 cryotomography of measles virus reveals how matrix protein coats the ribonucleocapsid
1088 within intact virions. Proc. Natl. Acad. Sci. U. S. A. *108*, 18085–18090.

1089 Liljeroos, L., Krzyzaniak, M.A., Helenius, A., and Butcher, S.J. (2013). Architecture of
1090 respiratory syncytial virus revealed by electron cryotomography. Proc. Natl. Acad. Sci. U. S.
1091 A. *110*, 11133–11138.

1092 Liu, J., Bartesaghi, A., Borgnia, M.J., Sapiro, G., and Subramaniam, S. (2008). Molecular
1093 architecture of native HIV-1 gp120 trimers. Nature *455*, 109–113.

1094 Lok, S.-M., Kostyuchenko, V., Nybakken, G.E., Holdaway, H.A., Battisti, A.J., Sukupolvi-
1095 Petty, S., Sedlak, D., Fremont, D.H., Chipman, P.R., Roehrig, J.T., et al. (2008). Binding of a
1096 neutralizing antibody to dengue virus alters the arrangement of surface glycoproteins. Nat.
1097 Struct. Mol. Biol. *15*, 312–317.

1098 Loney, C., Mottet-Osman, G., Roux, L., and Bhella, D. (2009). Paramyxovirus ultrastructure
1099 and genome packaging: cryo-electron tomography of sendai virus. J. Virol. *83*, 8191–8197.

1100 Long, F., Fong, R.H., Austin, S.K., Chen, Z., Klose, T., Fokine, A., Liu, Y., Porta, J.,
1101 Sapparapu, G., Akahata, W., et al. (2015). Cryo-EM structures elucidate neutralizing
1102 mechanisms of anti-chikungunya human monoclonal antibodies with therapeutic activity.
1103 Proc. Natl. Acad. Sci. U. S. A. *112*, 13898–13903.

Long, F., Doyle, M., Fernandez, E., Miller, A.S., Klose, T., Sevvana, M., Bryan, A., Davidson, E., Doranz, B.J., Kuhn, R.J., et al. (2019). Structural basis of a potent human monoclonal antibody against Zika virus targeting a quaternary epitope. Proc. Natl. Acad. Sci. U. S. A. *116*, 1591–1596.

Mancini, E.J., Clarke, M., Gowen, B.E., Rutten, T., and Fuller, S.D. (2000). Cryo-electron microscopy reveals the functional organization of an enveloped virus, Semliki Forest virus. Mol. Cell *5*, 255–266.

Mattei, S., Glass, B., Hagen, W.J.H., Kräusslich, H.-G., and Briggs, J.A.G. (2016). The structure and flexibility of conical HIV-1 capsids determined within intact virions. Science *354*, 1434–1437.

Mlakar, J., Korva, M., Tul, N., Popović, M., Poljšak-Prijatelj, M., Mraz, J., Kolenc, M., Resman Rus, K., Vesnaver Vipotnik, T., Fabjan Vodušek, V., et al. (2016). Zika Virus Associated with Microcephaly. N. Engl. J. Med. *374*, 951–958.

Modis, Y., Ogata, S., Clements, D., and Harrison, S.C. (2004). Structure of the dengue virus envelope protein after membrane fusion. Nature *427*, 313–319.

Neuman, B.W., Adair, B.D., Yoshioka, C., Quispe, J.D., Orca, G., Kuhn, P., Milligan, R.A., Yeager, M., and Buchmeier, M.J. (2006). Supramolecular architecture of severe acute respiratory syndrome coronavirus revealed by electron cryomicroscopy. J. Virol. *80*, 7918–7928.

Ono, A., and Freed, E.O. (2001). Plasma membrane rafts play a critical role in HIV-1 assembly and release. Proc. Natl. Acad. Sci. U. S. A. *98*, 13925–13930.

Overby, A.K., Pettersson, R.F., Grünewald, K., and Huiskonen, J.T. (2008). Insights into bunyavirus architecture from electron cryotomography of Uukuniemi virus. Proc. Natl. Acad. Sci. U. S. A. *105*, 2375–2379.

Park, G.W., Linden, K.G., and Sobsey, M.D. (2011). Inactivation of murine norovirus, feline calicivirus and echovirus 12 as surrogates for human norovirus (NoV) and coliphage (F) MS2 by ultraviolet light (254 nm) and the effect of cell association on UV inactivation. Lett. Appl. Microbiol. *52*, 162–167.

Porta, J., Jose, J., Roehrig, J.T., Blair, C.D., Kuhn, R.J., and Rossmann, M.G. (2014). Locking and blocking the viral landscape of an alphavirus with neutralizing antibodies. J. Virol. *88*, 9616–9623.

Porta, J., Mangala Prasad, V., Wang, C.-I., Akahata, W., Ng, L.F.P., and Rossmann, M.G. (2016). Structural Studies of Chikungunya Virus-Like Particles Complexed with Human Antibodies: Neutralization and Cell-to-Cell Transmission. J. Virol. *90*, 1169–1177.

Prasad, V.M., Miller, A.S., Klose, T., Sirohi, D., Buda, G., Jiang, W., Kuhn, R.J., and Rossmann, M.G. (2017). Structure of the immature Zika virus at 9 Å resolution. Nat. Struct. Mol. Biol. *24*, 184–186.

Pryce, R., Ng, W.M., Zeltina, A., Watanabe, Y., El Omari, K., Wagner, A., and Bowden, T.A. (2019). Structure-Based Classification Defines the Discrete Conformational Classes Adopted by the Arenaviral GP1. J. Virol. *93*.

Punch, E.K., Hover, S., Blest, H.T.W., Fuller, J., Hewson, R., Fontana, J., Mankouri, J., and Barr, J.N. (2018). Potassium is a trigger for conformational change in the fusion spike of an enveloped RNA virus. J. Biol. Chem. *293*, 9937–9944.

Renner, M., Flanagan, A., Dejnirattisai, W., Puttikhunt, C., Kasinrerk, W., Supasa, P., Wongwiwat, W., Chawansuntati, K., Duangchinda, T., Cowper, A., et al. (2018). Characterization of a potent and highly unusual minimally enhancing antibody directed against dengue virus. Nat. Immunol. *19*, 1248–1256.

Rey, F.A., Heinz, F.X., Mandl, C., Kunz, C., and Harrison, S.C. (1995). The envelope glycoprotein from tick-borne encephalitis virus at 2 A resolution. Nature *375*, 291–298.

Rissanen, I., Stass, R., Zeltina, A., Li, S., Hepojoki, J., Harlos, K., Gilbert, R.J.C., Huiskonen, J.T., and Bowden, T.A. (2017). Structural Transitions of the Conserved and Metastable Hantaviral Glycoprotein Envelope. J. Virol. *91*.

Ruigrok, R.W., Wrigley, N.G., Calder, L.J., Cusack, S., Wharton, S.A., Brown, E.B., and Skehel, J.J. (1986). Electron microscopy of the low pH structure of influenza virus haemagglutinin. EMBO J. *5*, 41–49.

San Martín, C., Huiskonen, J.T., Bamford, J.K.H., Butcher, S.J., Fuller, S.D., Bamford, D.H., and Burnett, R.M. (2002). Minor proteins, mobile arms and membrane-capsid interactions in the bacteriophage PRD1 capsid. Nat. Struct. Biol. *9*, 756–763.

Sevvana, M., Long, F., Miller, A.S., Klose, T., Buda, G., Sun, L., Kuhn, R.J., and Rossmann, M.G. (2018). Refinement and Analysis of the Mature Zika Virus Cryo-EM Structure at 3.1 Å Resolution. Structure *26*, 1169–1177.e3.

Shankar, S., Whitby, L.R., Casquilho-Gray, H.E., York, J., Boger, D.L., and Nunberg, J.H. (2016). Small-Molecule Fusion Inhibitors Bind the pH-Sensing Stable Signal Peptide-GP2 Subunit Interface of the Lassa Virus Envelope Glycoprotein. J. Virol. *90*, 6799–6807.

Sherman, M.B., Trujillo, J., Leahy, I., Razmus, D., Dehate, R., Lorcheim, P., Czarneski, M.A., Zimmerman, D., Newton, J.T.M., Haddow, A.D., et al. (2013). Construction and organization of a BSL-3 cryo-electron microscopy laboratory at UTMB. J. Struct. Biol. *181*, 223–233.

Sirohi, D., Chen, Z., Sun, L., Klose, T., Pierson, T.C., Rossmann, M.G., and Kuhn, R.J. (2016). The 3.8 Å resolution cryo-EM structure of Zika virus. Science *352*, 467–470.

Skehel, J.J., Bayley, P.M., Brown, E.B., Martin, S.R., Waterfield, M.D., White, J.M., Wilson, I.A., and Wiley, D.C. (1982). Changes in the conformation of influenza virus hemagglutinin at the pH optimum of virus-mediated membrane fusion. Proc. Natl. Acad. Sci. U. S. A. *79*, 968–972.

Strauss, J.D., Hammonds, J.E., Yi, H., Ding, L., Spearman, P., and Wright, E.R. (2016). Three-Dimensional Structural Characterization of HIV-1 Tethered to Human Cells. J. Virol. *90*, 1507–1521.

Subramaniam, S., Bartesaghi, A., Liu, J., Bennett, A.E., and Sougrat, R. (2007). Electron tomography of viruses. Curr. Opin. Struct. Biol. *17*, 596–602.

Sukupolvi-Petty, S., Brien, J.D., Austin, S.K., Shrestha, B., Swayne, S., Kahle, K., Doranz, B.J., Johnson, S., Pierson, T.C., Fremont, D.H., et al. (2013). Functional analysis of antibodies against dengue virus type 4 reveals strain-dependent epitope exposure that impacts neutralization and protection. J. Virol. *87*, 8826–8842.

Sun, S., Xiang, Y., Akahata, W., Holdaway, H., Pal, P., Zhang, X., Diamond, M.S., Nabel, G.J., and Rossmann, M.G. (2013). Structural analyses at pseudo atomic resolution of Chikungunya virus and antibodies show mechanisms of neutralization. Elife *2*, e00435.

Sun, Z., El Omari, K., Sun, X., Ilca, S.L., Kotecha, A., Stuart, D.I., Poranen, M.M., and Huiskonen, J.T. (2017). Double-stranded RNA virus outer shell assembly by bona fide domain-swapping. Nat. Commun. *8*, 14814.

Teoh, E.P., Kukkaro, P., Teo, E.W., Lim, A.P.C., Tan, T.T., Yip, A., Schul, W., Aung, M., Kostyuchenko, V.A., Leo, Y.S., et al. (2012). The structural basis for serotype-specific neutralization of dengue virus by a human antibody. Sci. Transl. Med. *4*, 139ra83.

Thompson, R.F., Walker, M., Siebert, C.A., Muench, S.P., and Ranson, N.A. (2016). An introduction to sample preparation and imaging by cryo-electron microscopy for structural biology. Methods *100*, 3–15.

Tran, E.E.H., Simmons, J.A., Bartesaghi, A., Shoemaker, C.J., Nelson, E., White, J.M., and Subramaniam, S. (2014). Spatial localization of the Ebola virus glycoprotein mucin-like domain determined by cryo-electron tomography. J. Virol. *88*, 10958–10962.

Tran, E.E.H., Nelson, E.A., Bonagiri, P., Simmons, J.A., Shoemaker, C.J., Schmaljohn, C.S., Kobinger, G.P., Zeitlin, L., Subramaniam, S., and White, J.M. (2016). Mapping of Ebolavirus Neutralization by Monoclonal Antibodies in the ZMapp Cocktail Using Cryo-Electron Tomography and Studies of Cellular Entry. J. Virol. *90*, 7618–7627.

Veesler, D., Ng, T.-S., Sendamarai, A.K., Eilers, B.J., Lawrence, C.M., Lok, S.-M., Young, M.J., Johnson, J.E., and Fu, C.-Y. (2013). Atomic structure of the 75 MDa extremophile Sulfolobus turreted icosahedral virus determined by CryoEM and X-ray crystallography. Proc. Natl. Acad. Sci. U. S. A. *110*, 5504–5509.

Wang, J., and Moore, P.B. (2017). On the interpretation of electron microscopic maps of biological macromolecules. Protein Sci. *26*, 122–129.

Wang, Q., Bosch, B.-J., Vlak, J.M., van Oers, M.M., Rottier, P.J., and van Lent, J.W.M. (2016a). Budded baculovirus particle structure revisited. J. Invertebr. Pathol. *134*, 15–22.

Wang, Q., Yang, H., Liu, X., Dai, L., Ma, T., Qi, J., Wong, G., Peng, R., Liu, S., Li, J., et al. (2016b). Molecular determinants of human neutralizing antibodies isolated from a patient infected with Zika virus. Sci. Transl. Med. *8*, 369ra179.

Wang, X., Li, S.-H., Zhu, L., Nian, Q.-G., Yuan, S., Gao, Q., Hu, Z., Ye, Q., Li, X.-F., Xie, D.-Y., et al. (2017). Near-atomic structure of Japanese encephalitis virus reveals critical determinants of virulence and stability. Nat. Commun. *8*, 14.

Weaver, S.C., Charlier, C., Vasilakis, N., and Lecuit, M. (2018). Zika, Chikungunya, and Other Emerging Vector-Borne Viral Diseases. Annu. Rev. Med. *69*, 395–408.

Wei, H., Holland Cheng, R., Berriman, J., Rice, W.J., Stokes, D.L., Katz, A., Morgan, D.G., and Gottlieb, P. (2009). Three-Dimensional Structure of the Enveloped Bacteriophage Φ12: An Incomplete T = 13 Lattice Is Superposed on an Enclosed T = 1 Shell. PLoS One *4*, e6850.

Welsch, S., Kolesnikova, L., Krähling, V., Riches, J.D., Becker, S., and Briggs, J.A.G. (2010). Electron tomography reveals the steps in filovirus budding. PLoS Pathog. *6*, e1000875.

Wilson, I.A., Skehel, J.J., and Wiley, D.C. (1981). Structure of the haemagglutinin membrane glycoprotein of influenza virus at 3 A resolution. Nature *289*, 366–373.

Wirawan, M., Fibriansah, G., Marzinek, J.K., Lim, X.X., Ng, T.-S., Sim, A.Y.L., Zhang, Q.,

1232 Kostyuchenko, V.A., Shi, J., Smith, S.A., et al. (2018). Mechanism of Enhanced Immature
1233 Dengue Virus Attachment to Endosomal Membrane Induced by prM Antibody. Structure.

1234 Wolf, M., DeRosier, D.J., and Grigorieff, N. (2006). Ewald sphere correction for single-
1235 particle electron microscopy. Ultramicroscopy *106*, 376–382.

1236 Xiao, C., and Rossmann, M.G. (2011). Structures of giant icosahedral eukaryotic dsDNA
1237 viruses. Curr. Opin. Virol. *1*, 101–109.

1238 Xiao, C., Kuznetsov, Y.G., Sun, S., Hafenstein, S.L., Kostyuchenko, V.A., Chipman, P.R.,
1239 Suzan-Monti, M., Raoult, D., McPherson, A., and Rossmann, M.G. (2009). Structural studies
1240 of the giant mimivirus. PLoS Biol. *7*, e92.

1241 Xiao, C., Fischer, M.G., Bolotaulo, D.M., Ulloa-Rondeau, N., Avila, G.A., and Suttle, C.A.
1242 (2017). Cryo-EM reconstruction of the Cafeteria roenbergensis virus capsid suggests novel
1243 assembly pathway for giant viruses. Sci. Rep. *7*, 5484.

1244 Xu, K., Chan, Y.-P., Bradel-Tretheway, B., Akyol-Ataman, Z., Zhu, Y., Dutta, S., Yan, L.,
1245 Feng, Y., Wang, L.-F., Skiniotis, G., et al. (2015). Crystal Structure of the Pre-fusion Nipah
1246 Virus Fusion Glycoprotein Reveals a Novel Hexamer-of-Trimers Assembly. PLoS Pathog.
1247 *11*, e1005322.

1248 Yamauchi, Y., and Helenius, A. (2013). Virus entry at a glance. J. Cell Sci. *126*, 1289–1295.

1249 Yan, X., Chipman, P.R., Castberg, T., Bratbak, G., and Baker, T.S. (2005). The marine algal
1250 virus PpV01 has an icosahedral capsid with T=219 quasisymmetry. J. Virol. *79*, 9236–9243.

1251 Ye, Y., Chang, P.H., Hartert, J., and Wigginton, K.R. (2018). Reactivity of Enveloped Virus
1252 Genome, Proteins, and Lipids with Free Chlorine and UV254. Environ. Sci. Technol. *52*,
1253 7698–7708.

1254 Zanetti, G., Briggs, J.A.G., Grünewald, K., Sattentau, Q.J., and Fuller, S.D. (2006). Cryo-
1255 electron tomographic structure of an immunodeficiency virus envelope complex in situ. PLoS
1256 Pathog. *2*, e83.

1257 Zhang, S., Kostyuchenko, V.A., Ng, T.-S., Lim, X.-N., Ooi, J.S.G., Lambert, S., Tan, T.Y.,
1258 Widman, D.G., Shi, J., Baric, R.S., et al. (2016). Neutralization mechanism of a highly potent
1259 antibody against Zika virus. Nat. Commun. *7*, 13679.

1260 Zhang, W., Chipman, P.R., Corver, J., Johnson, P.R., Zhang, Y., Mukhopadhyay, S., Baker,
1261 T.S., Strauss, J.H., Rossmann, M.G., and Kuhn, R.J. (2003a). Visualization of membrane
1262 protein domains by cryo-electron microscopy of dengue virus. Nat. Struct. Biol. *10*, 907–912.

1263 Zhang, X., Xiang, Y., Dunigan, D.D., Klose, T., Chipman, P.R., Van Etten, J.L., and
1264 Rossmann, M.G. (2011). Three-dimensional structure and function of the Paramecium
1265 bursaria chlorella virus capsid. Proc. Natl. Acad. Sci. U. S. A. *108*, 14837–14842.

1266 Zhang, X., Ge, P., Yu, X., Brannan, J.M., Bi, G., Zhang, Q., Schein, S., and Zhou, Z.H.
1267 (2013a). Cryo-EM structure of the mature dengue virus at 3.5-Å resolution. Nat. Struct. Mol.
1268 Biol. *20*, 105–110.

1269 Zhang, X., Sheng, J., Plevka, P., Kuhn, R.J., Diamond, M.S., and Rossmann, M.G. (2013b).
1270 Dengue structure differs at the temperatures of its human and mosquito hosts. Proc. Natl.
1271 Acad. Sci. U. S. A. *110*, 6795–6799.

1272 Zhang, X., Sheng, J., Austin, S.K., Hoornweg, T.E., Smit, J.M., Kuhn, R.J., Diamond, M.S.,
1273 and Rossmann, M.G. (2015). Structure of acidic pH dengue virus showing the fusogenic

glycoprotein trimers. J. Virol. *89*, 743–750.

Zhang, Y., Corver, J., Chipman, P.R., Zhang, W., Pletnev, S.V., Sedlak, D., Baker, T.S., Strauss, J.H., Kuhn, R.J., and Rossmann, M.G. (2003b). Structures of immature flavivirus particles. EMBO J. *22*, 2604–2613.

Zhong, Q., Carratalà, A., Nazarov, S., Guerrero-Ferreira, R.C., Piccinini, L., Bachmann, V., Leiman, P.G., and Kohn, T. (2016). Genetic, Structural, and Phenotypic Properties of MS2 Coliphage with Resistance to ClO Disinfection. Environ. Sci. Technol. *50*, 13520–13528.

Zhu, P., Chertova, E., Bess, J., Jr, Lifson, J.D., Arthur, L.O., Liu, J., Taylor, K.A., and Roux, K.H. (2003). Electron tomography analysis of envelope glycoprotein trimers on HIV and simian immunodeficiency virus virions. Proc. Natl. Acad. Sci. U. S. A. *100*, 15812–15817.

Zhu, P., Liu, J., Bess, J., Jr, Chertova, E., Lifson, J.D., Grisé, H., Ofek, G.A., Taylor, K.A., and Roux, K.H. (2006). Distribution and three-dimensional structure of AIDS virus envelope spikes. Nature *441*, 847–852.